Journal of Constructional Steel Research 204 (2023) 107842

Contents lists available at ScienceDirect

Journal of Constructional Steel Research

journal homepage: www.elsevier.com/locate/jcsr

Improving structural robustness of steel frame buildings by enhancing floor deck connections

Junjie Wang [a,b], Ke Ke [c,*], Michael C.H. Yam [b,d], Minghong Teng [c], Wei Wang [e]

[a] School of Civil Engineering, Shandong University, Jinan, Shandong, China
[b] Department of Building and Real Estate, Hong Kong Polytechnic University, Hong Kong, China
[c] School of Civil Engineering, Chongqing University, Chongqing, China
[d] Chinese National Engineering Research Centre for Steel Construction (Hong Kong Branch), The Hong Kong Polytechnic University, Hong Kong, China
[e] Department of Structural Engineering, Tongji University, Shanghai, China

ARTICLE INFO

Keywords:
Composite slab
Profiled steel deck
Steel frame
Progressive collapse
Disproportionate collapse
Robustness

ABSTRACT

In current composite floors, the strength of the deck connections restraining the profiled steel decks to the floor beams or to the neighboring steel decks are much weaker compared with the sectional strength of the steel deck, which would limit the load-carrying capacity of the composite floors under progressive collapse scenarios. Given this, this study proposed two novel types of enhanced deck connections for improving the load-carrying behavior of the deck-to-beam connection and deck-to-deck connection. Based on a 5-story steel prototype building, the feasibility of the proposed deck connections in improving the progressive collapse resistance was validated by comparing with the common practice of the deck connections via a reduced-order (RO) modeling approach. The structural robustness of the prototype building in the case of sudden column removal was evaluated and discussed. Compared with the commonly used deck connections, the enhanced deck connections could improve the structural robustness of the prototype building by 27%.

1. Introduction

In steel construction, frame building structures are widely used in residential and industrial systems [1–5]. The vital role of the composite slab in enhancing the progressive collapse resistance of steel frame structures has been verified by previous studies at the beam-to-column connection level [6–9] and the floor substructure level [10–18]. In addition to the flexural resistance of composite slabs [19–21], tensile membrane actions of composite slabs can be developed to redistribute the gravity load to the neighboring structure [16,18], which is mainly attributed to the contribution by rebars and profiled steel decks [22–24]. According to the cross-sectional shape of profiled steel deck, composite slabs can be classified into four categories [23]: trapezoidal, dovetail, reentrant, or rebar-truss composite slab (Fig. 1). In China, the profiled steel decks in these composite slabs are restrained to the floor beams through welded shear studs, bolted shear connectors, or spot-welding. For the side laps between the neighboring profiled steel decks, the trapezoidal, dovetail, and reentrant steel decks are generally fixed with screws or rivets, while the rebar-truss steel decks are mostly locked together by mechanically clasping their curled edges together (Fig. 2). However, the strength of these deck connections is usually much weaker than the cross-sectional strength of the profiled steel decks, which would limit the development of the tensile membrane action in the profiled steel decks [23,24]. If the steel deck is ideally continuous, the tensile membrane action of the composite slabs contributed by the composite action between the concrete and steel [25–29] could be significantly enhanced, and the progressive collapse resistance of the entire steel frame building would also be improved [22,23]. Hence, it is beneficial to develop reliable and feasible deck connections to improve the tensile membrane action of the profiled steel decks.

Apart from the weak deck connections, the corrugated cross-section geometry of the trapezoidal, dovetail and reentrant steel decks (Fig. 1) also limited their tensile membrane force in their transverse directions (y direction) [24]. On the contrary, if the deck connections' performance is improved, the flat shape of the rebar-tuss steel deck (Fig. 1) would be conducive to the development of the steel decks' tensile membrane force in both longitudinal (x) and transverse (y) directions. In light of the above, enhanced deck connections were developed in this study based on the rebar-truss steel decks, and the corresponding enhancing methodology is illustrated in Fig. 2.

* Corresponding author.
E-mail address: ke.ke@cqu.edu.cn (K. Ke).

https://doi.org/10.1016/j.jcsr.2023.107842
Received 9 November 2022; Received in revised form 19 January 2023; Accepted 30 January 2023
Available online 14 February 2023

By comparing with the commonly used deck connections, the feasibility of the enhanced deck connections in improving the in-plane tensile performance of the profiled steel decks can be verified at the component level. However, considering the complexity of the progressive collapse phenomenon, it would be more reliable and accurate to assess the effect of the enhanced deck connections at the overall structural level [30,31]. Nevertheless, the full-scale structural system testing [32,33] is overly expensive, complex and time-consuming; hence, numerical analysis would be a practicable way to analyze the structural performance of a steel frame building under progressive collapse scenarios. In addition, due to the high computational cost of high-fidelity (HF) models, the reduced-order (RO) models are usually adopted to simulate the progressive collapse behavior of steel frame buildings [23,34–38], offering a compelling tool for the current work.

To explore the rationality of the proposed enhanced deck connections and their influences on the progressive collapse resistance of the structural system, a prototype 5-story steel frame building was developed using codified design methods. The influence of the enhanced deck connections on improving the progressive collapse resistance of this prototype building was investigated using the RO modeling approach. The LS-DYNA software [39] was used to perform all the numerical simulations in this study.

2. Prototype building

According to Chinese codes [40–44], a 5-story steel moment-resisting frame building was designed (Fig. 3a), and all the analyses in the following section were performed based on it. There were four equal spans in both the *x* and *y* directions. The span lengths of girders and beams were both 6 m, while the beam spacing was 3 m. The story height was 4.5 m. The span length, beam spacing, and story height were all determined according to common practice in China [28]. This prototype building was designed by assuming the gravity loading as 5 kN/m^2 dead load (DL) and 2 kN/m^2 live load (LL) according to [34,42]. The design basic earthquake acceleration was 0.05 times the gravitational acceleration. Both girders and beams were designed to be H-shaped H300 × 150 × 6.5 × 9 steel section. The girder-to-column connections were welded-flange-bolted-web connections, while the beam-to-girder connection was designed as typical bolted shear tab connections, as schematically shown in Fig. 3b. Since the girders in the two perpendicular directions were both rigidly connected to the column, it was recommended to use the rectangular tube section in this case, as their bi-directional flexural properties are relatively close. Hence, the steel column was designed to be 350 × 350 × 10 square tube section. These connections were fastened by Grade 10.9 M20 high-strength bolts.

Rebar-truss composite slabs [23,44] were used to develop the flooring system of the prototype building (Fig. 3c). The rebar-truss was laid in the *x* direction (girder axis direction), while the center-to-center spacing was 200 mm. The rebar-trusses were restrained to the steel decks' small ribs through resistance spot welding. The concrete cover of the slab bars was 15 mm. The steel deck's thickness was 1.2 mm. The length and width of each rebar-truss steel deck were 6 m and 0.6 m, respectively. The steel decks were fixed to the beam top flanges through bolted shear connectors (Fig. 3b), and the adjacent steel decks were mechanically locked together by the curled edges (i.e. clasped connection in Fig. 2). Grade 10.9 M20 bolted shear connectors with a length of 80 mm were used in the prototype building, which could enable the demounting and recycling of the floor beams and slabs at the end of service life [45]. In addition, compared with the welded shear studs, the bolted shear connectors also facilitated fixing the proposed steel deck connection to the structural beams and applying axial preload, which will be presented in the next section. Each girder and beam both had 56 shear connectors, and full composite action was achieved. These shear connectors were arranged in two rows (Fig. 3b).

Q345 Grade steel was used for the steel frames and steel decks. Grade CRB550 cold-rolled bars [46,47] and Grade C30 concrete [48] were used for slab reinforcement and slab, respectively. Note that in the construction process, fillers may be adopted to improve the flowability [49,50], passing ability [51,52] and at the same time, to reduce the shear thickening [53–55] of the concrete so that the designed concrete could pass through the narrow gap of reinforcement and shear connectors, thus deficiency of the composite slabs was not considered in the current work. The bolted shear connectors and bolts were made of Grade 10.9 steel [40,43]. The steel and concrete material properties are shown in Fig. 4, which are identical to that used in Ref. [23].

3. Numerical investigation of deck connections

3.1. Steel deck connections

In this study, the commonly used deck-to-beam connection with bolted shear connectors was named as shear connection, while the mechanically clasped connection between neighboring profiled steel decks was named as clasped connections, as shown in Fig. 2. For the novel deck connections, the deck-to-beam connection was enhanced by fixing the folded deck edges to the shear connectors on the beam top flanges via flat shear plates (Fig. 6a), designated as the "folded connection". The deck-to-deck connection was strengthened by fastening the neighboring folded deck edges via steel angles and high-strength bolts (Fig. 6b), which is labeled as the "angle connection". Fig. 5 and Fig. 6 illustrate the detailed dimensions of these deck connections.

In the folded connection (Fig. 6a), a shear plate was used to transfer the steel decks' in-plane tension to shear connectors. The shear plate size was designed to meet the following requirements: i) bolt hole failure should be later than the steel deck's sectional tensile fracture; ii) shear plate shall have sufficient bending resistance and stiffness to resist the bending moment caused by the steel deck's in-plane tension; iii) bolt

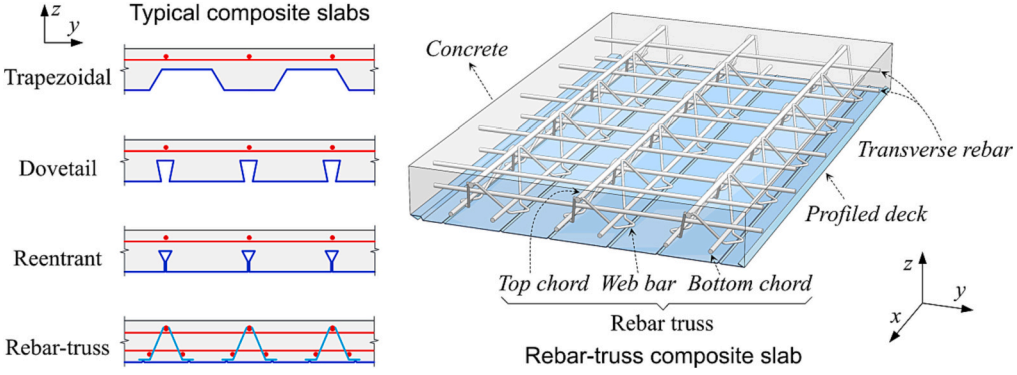

Fig. 1. Typical composite slabs.

hole's edge distance shall meet the code's requirements [40]. In the angle connection (Fig. 6b), two equal leg angles and Grade 10.9 M16 bolts (200 mm spacing) were used to transfer the steel deck's in-plane tension between adjacent decks. The angle size was designed according to the following requirements: i) angle should have sufficient bending resistance and stiffness to resist the bending moment caused by the steel deck's in-plane tension; ii) bolt hole failure shall be later than the bolt's tensile fracture; iii) bolt hole's edge distance shall meet the code's requirements and the bolt hole should have sufficient installation space for the bolt wrench [40]; iv) the height of the angle should be lower than the height of the upper transverse rebar.

To examine the effect of the folded degree of the deck edges, various folded configurations were designed, as schematically shown in Fig. 6. According to the folded degree, the three designed folded connections (Fig. 6a) were coded as "half-fold" connection, "tri-fold-1" connection and "tri-fold-2" connection, respectively. For the angle connection, four connections (Fig. 6b) were coded as "half-fold" connection, "tri-fold" connection, "gate-fold-1" connection and "gate-fold-2" connection, respectively. Apart from the folded configurations, the preload effect of the connectors and bolts was also investigated. Note that the recommended preload of Grade 10.9 high-strength bolts is approximately 600 MPa [40]. Hence, three preload degrees, 0, 300 MPa and 600 MPa, were applied to the shear connectors and bolts to develop the parameter matrix.

3.2. Numerical models of deck connections

LS-DYNA was used to develop the HF models of the designed deck connections, as shown in Figs. 5 and 6, which were used to investigate and compare their structural performance in transferring the tensile load. The steel decks were modeled by shell elements, while the steel plates, angles, and shear connectors were modeled by solid elements. The blue dashed curve in Fig. 4, which was obtained by coupon tests of a steel plate (Grade Q345 steel with the measured yield strength of 419 MPa), was used to model the steel plates and angles. For these deck connection models, the fracture simulation of the steel deck was a critical issue that may greatly affect the accuracy of the simulation results. Therefore, the fracture model of the steel deck was first calibrated according to the corresponding coupon test results of steel deck.

3.2.1. Fracture model of steel deck

As illustrated in Fig. 7, two types of coupon specimens were designed, including flat plate and hole plate. The test result of flat plate was firstly used to obtain the nominal stress-strain curve of steel deck, which was shown in Fig. 4 and Fig. 7a. Then, the true stress-strain curve of the steel deck could be derived from the nominal stress-strain curve (Fig. 7a) following the approach described in Ref. [56]. The Rice-Tracey fracture model (RT model) [57], $\varepsilon_f = ae^{-b\eta}$, was adopted to simulate the fracture behavior of the steel. In this model, ε_f was plastic fracture strain, η was stress triaxiality, which was found to be a significant coefficient in simulating fracture [58–60], while "a" and "b" were model parameters needed to be determined by the coupon test results. Given the symmetry of the model, the corresponding quarter models were built for both flat plate and hole plate specimens using shell elements (Fig. 7b). The element size at the core region was chosen as 0.5 mm, which was confirmed by a mesh sensitivity analysis [61,62]. According to the calibration approach described in Ref. [56], the RT model was calibrated as $\varepsilon_f = 1.07e^{-1.68\eta}$. As shown in Fig. 7b, the simulation results using the calibrated RT model well matched the test results of flat plate and hole plate specimens.

As mentioned above, the fracture model was calibrated using a 0.5 mm mesh size. But it would be time-consuming to use this relatively small mesh size to simulate the deck connection. To enable the calibrated fracture model to be used for the deck connection models with relatively large mesh sizes, a mesh-size scaling function $i(l_c)$ was used to adjust it. Thus, the calibrated RT model became $\varepsilon_f = 1.07e^{-1.68\eta} \cdot i(l_c)$. $i(l_c)$ defined the plastic failure strain as a function of the initial element size, l_c, which was equal to a shell element's area divided by its longest side length. To calibrate $i(l_c)$, a notched plate model in Fig. 8 was adopted as the benchmark model. The notched plate was modeled with different sizes of shell elements, including 0.5 mm, 1 mm, 2 mm, and 3 mm, respectively. The 0.5 mm mesh size model was taken as the benchmark, while the corresponding scaling factor $i(l_c)$ for other mesh size models was calibrated based on the 0.5 mm mesh size model, and the calibrated $i(l_c)$ was shown in Fig. 8. Besides, the flat specimen was also modeled with varied mesh sizes from 0.5 mm to 3 mm, and all the flat specimen models fractured at the same displacement (Fig. 8), which validated the feasibility of the calibrated $i(l_c)$.

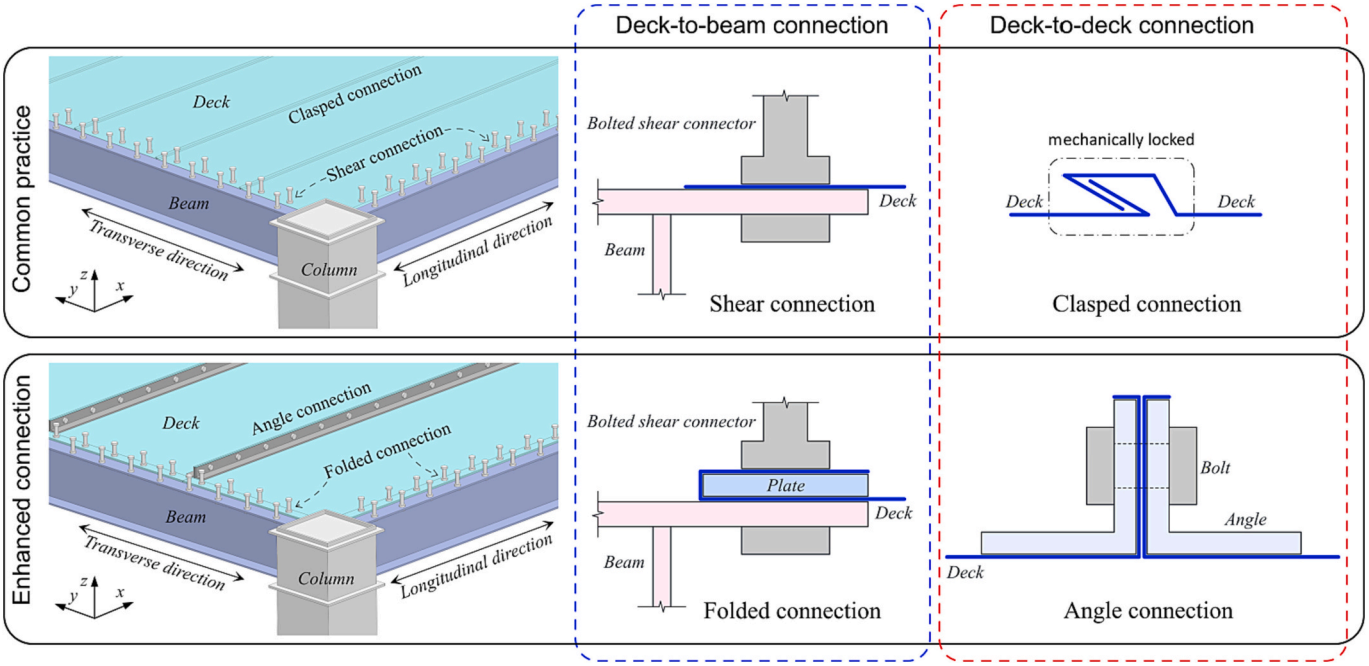

Fig. 2. Commonly used and enhanced floor deck connections.

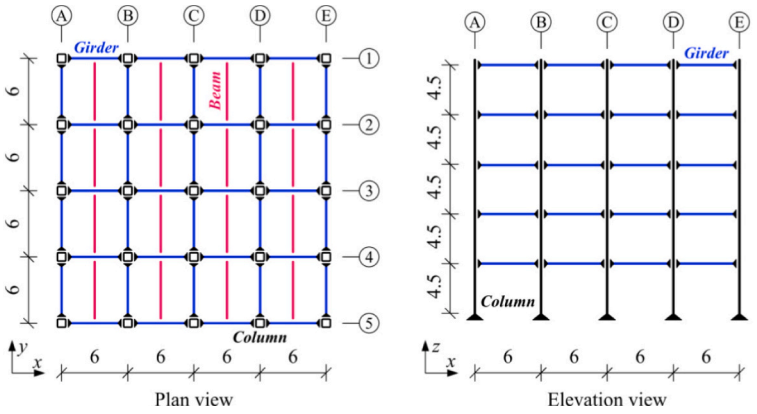

(a) Structural layout (unit: m)

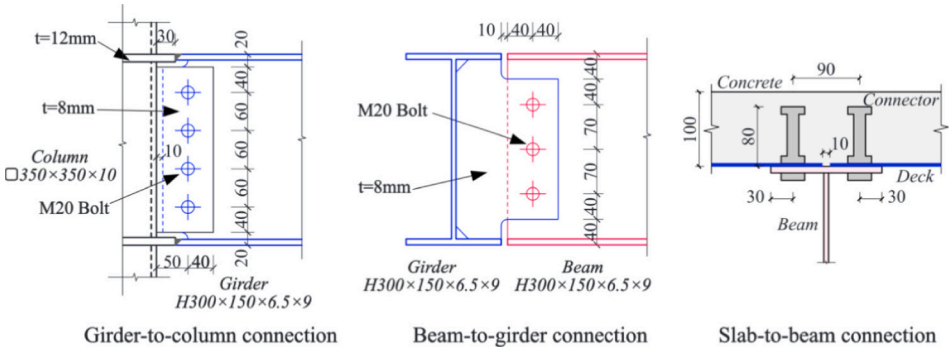

(b) Connection details (unit: mm)

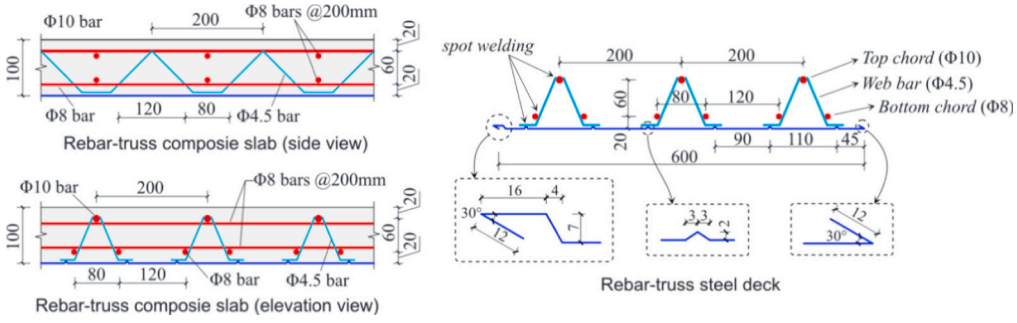

(c) Rebar-truss composite slabs (unit: mm)

Fig. 3. Prototype building.

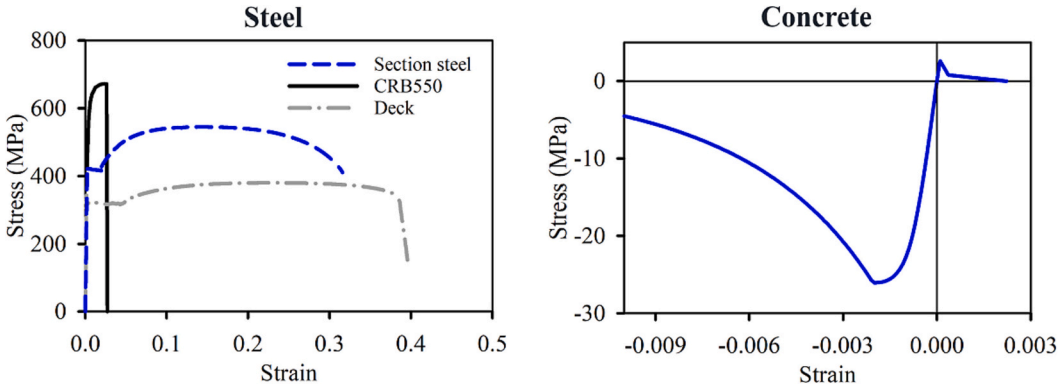

Fig. 4. Nominal stress-strain curves of materials.

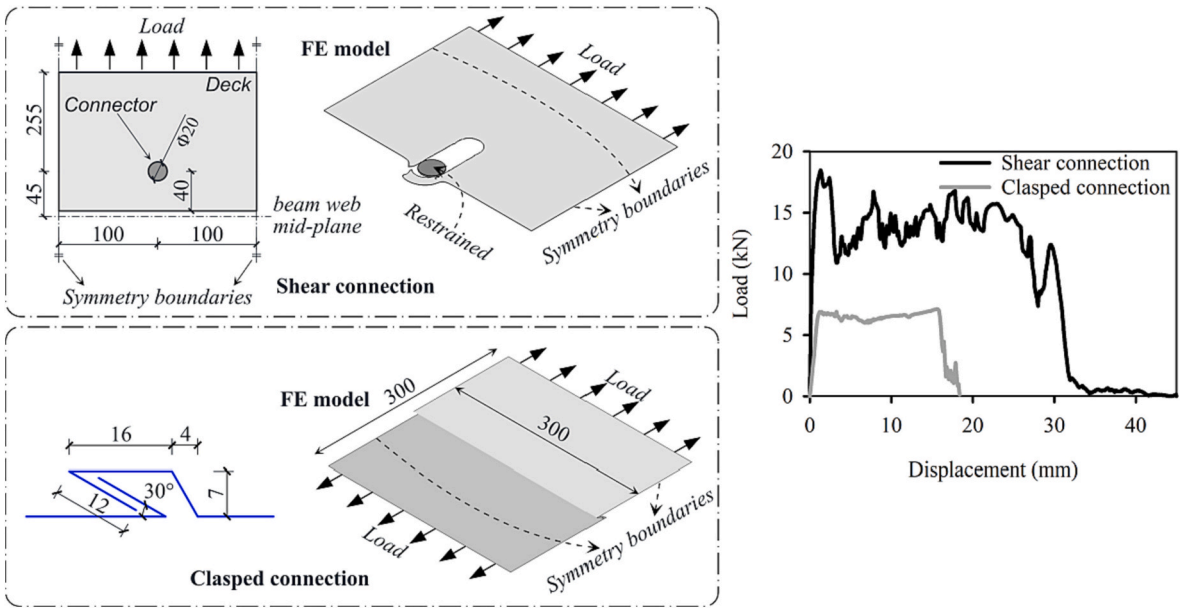

Fig. 5. HF models for conventional floor deck connections (unit: mm).

3.2.2. Deck connection models

The specific modeling details of each deck connection model are introduced as follows:

For the shear connection model (Fig. 5), the shear connector was simply modeled by a short rigid cylinder, which was completely restrained. The contact between the steel deck and the shear connector was modeled by the "Eroding-Nodes-to-Surface" contact. To simulate the constraint provided by the concrete slab, the out-of-plane displacement of the steel decks was fully restrained. For the clasped connection (Fig. 5), the contact between steel decks was modeled by the "Automatic-Single-Surface" contact.

In the folded connection model (Fig. 6a), i) the contact between deck and plate, ii) the contact between deck and beam, iii) the contact between plate and beam, iv) the contact between plate and shear connector, and v) the contact between beam and shear connector were all modeled by the "Automatic-Surface-to-Surface" contact, while the "Eroding-Nodes-to-Surface" contact was used to model the contact between the deck and the shear connector. For simplicity, only half part of the beam top flange was modeled (Fig. 6a), which is fully restrained at the face co-planar with the beam web's mid-plane. In the angle connection model (Fig. 6b), i) the contact between decks and angles and ii) the contact between angles and bolts were modeled by the "Automatic-Surface-to-Surface" contact, while the contact between the deck and the bolt was modeled by the "Eroding-Nodes-to-Surface" contact. The friction coefficient of contacting surfaces between these steel components was assumed to be 0.5 as per [22].

Symmetric constraints were applied to the symmetry boundaries of these deck connection models. Lateral tension was applied uniformly to the end edges of the steel decks (Figs. 5 and 6). It is worth noting that the modeling techniques mentioned above has been verified in previous studies conducted by Wang and colleagues [56].

3.3. Simulation results and discussion

The equivalent load-displacement curves of these deck connections at a width of 300 mm are shown in Figs. 5 and 6. The ultimate resistance, F_u, and the corresponding displacement, δ_u, are summarized in Table 1. Besides, the ratios between F_u and the nominal ultimate resistance of a 300 mm wide steel deck (i.e. R_u), are also listed in Table 1.

For the shear connection and clasped connection, their F_u/R_u ratios were 13.5% and 5.2%, respectively. The shear connection achieved its F_u, 18.5kN, at a displacement of 1.3 mm; then, its resistance remained at about 15 kN until its completely shear-out failure at a displacement of 29.6 mm (Fig. 5) was triggered. The load-carrying capacity of the clasped connection maintained between 6 kN and 7 kN throughout the loading process until F_u was reached at a displacement of 15.6 mm (Fig. 5), and then this connection failed completely when the two decks were detached from each other.

For the folded connection without preload, the F_u/R_u ratios of "half-fold" and "tri-fold-1" cases were 72.7% and 74.6%, respectively, which were greatly improved compared to the shear connection. However, the F_u of "half-fold" and "tri-fold-1" cases were both reached at a small displacement of 1.8 mm, and then the folded edges were straightened, resulting in a sudden decrease in the resistance. Compared with "tri-fold-1" case, the external folded surface of "tri-fold-2" case was longer and fixed by the shear connector, making it difficult to slide and deform freely (Fig. 6). Therefore, its load-carrying capacity could steadily increase in a relatively large deformation range until its F_u was achieved (20.8 mm), and its F_u/R_u ratio was 106.3%. After applying 300 MPa and 600 MPa preload in the shear connector, the F_u/R_u ratio of the tri-fold-2 case was increased to 116.9% and 119.8%, respectively, while the δ_u was also increased to 29.6 mm and 36.0 mm, respectively. The F_u/R_u ratio was greater than unity because the symmetrical boundary conditions were applied to the side deck edges in these connection models. In this context, during the simulation, the steel deck was in a bidirectional tensile stress state, resulting in F_u greater than R_u. For the tri-fold-2 with 600 MPa preload case, its F_u and δ_u were 8.9 and 20.2 times the shear connection, respectively.

For the angle connection without preload, the half-fold case did not fail prematurely like the "half-fold folded connection", and its F_u/R_u ratio could reach 100.7% at a displacement of 24.8 mm. This was because when the tensile loads were applied to the deck end edges, the two upper angle toes would press the steel decks in the middle, making it difficult to slide. The δ_u and F_u/R_u ratio of the tri-fold case were 36.0 mm and 110.4%, respectively, which were significantly improved compared with the half-fold case. While continuing to increase the folded degree to "gate-fold-1" and "gate-fold-2" cases, neither δ_u nor F_u/R_u was improved compared with "tri-fold" case. In addition, after applying 300 MPa and 600 MPa bolt preload, δ_u and F_u of "tri-fold" case did not improve significantly. This indicates that the proposed tri-fold angle connection may be sufficient to transfer the in-plane tension of steel decks. Note that the F_u and δ_u of the tri-fold configuration without preload case 20.3 and

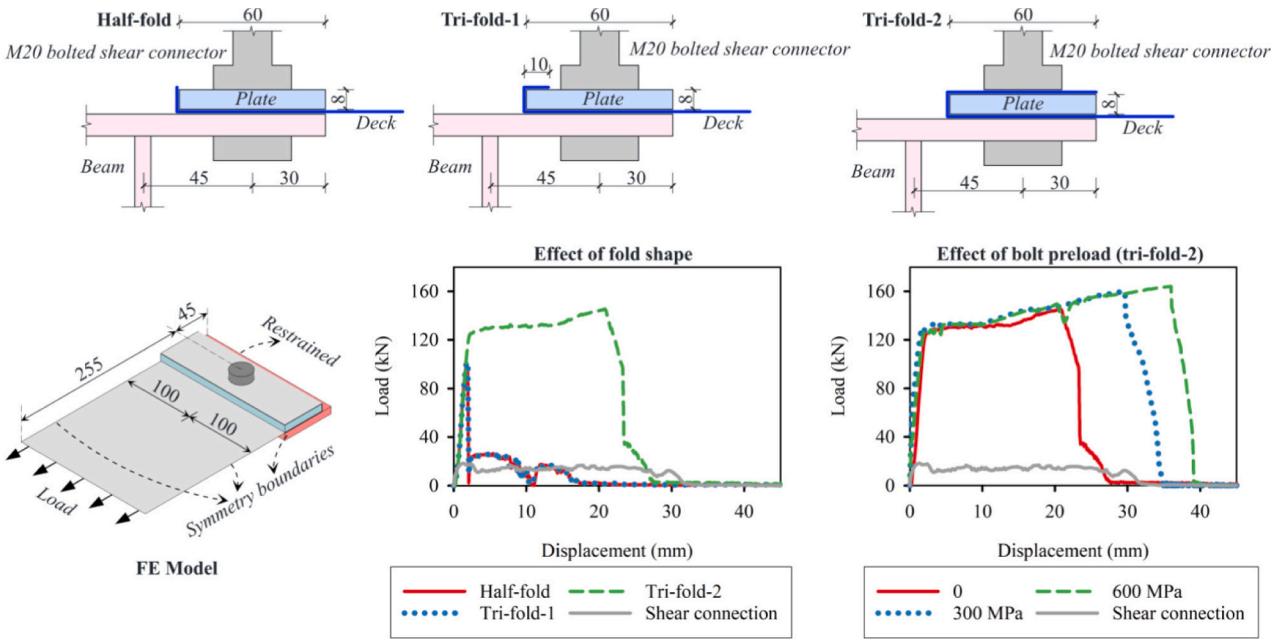

(a) Folded connection

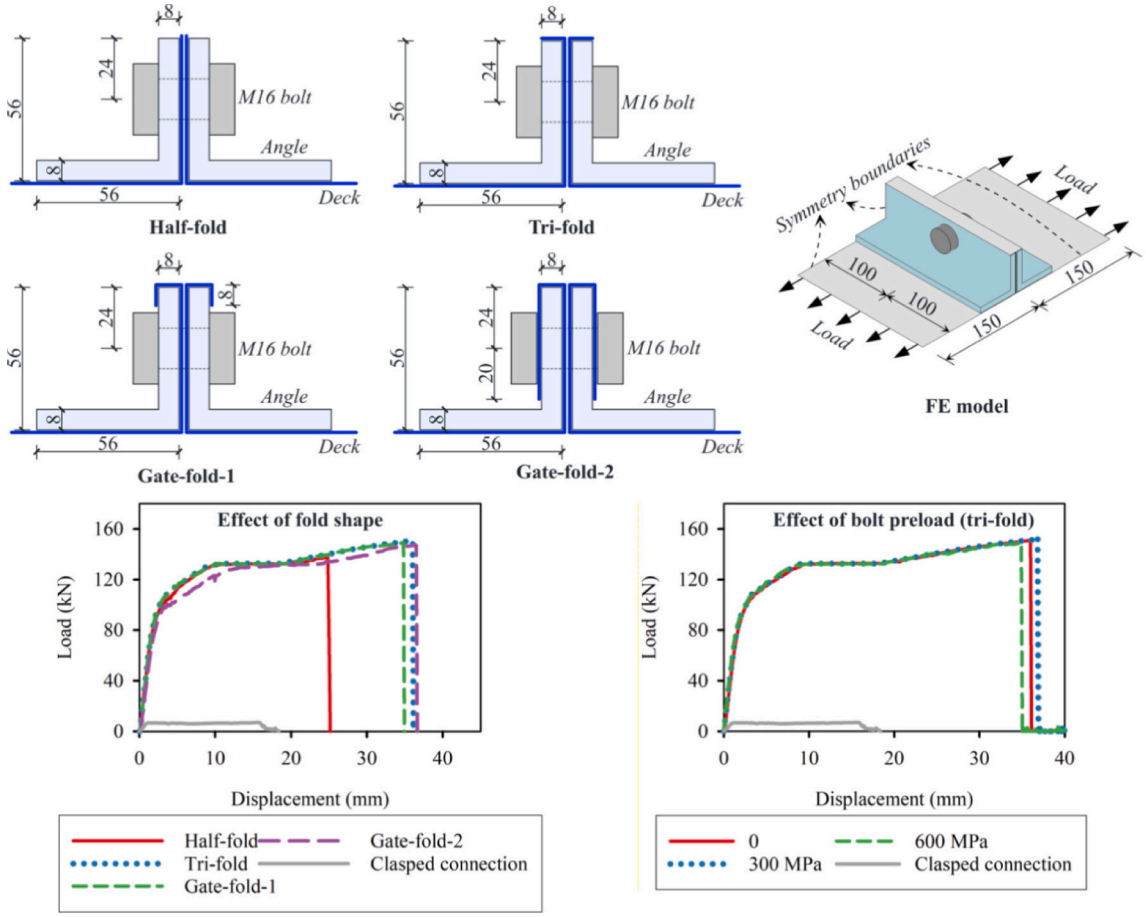

(b) Angle connection

Fig. 6. Enhanced floor deck connections (unit: mm).

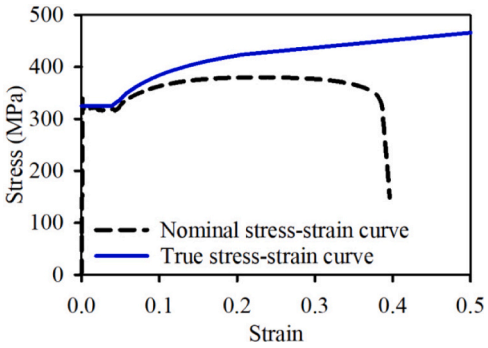

(a) True stress-strain curve

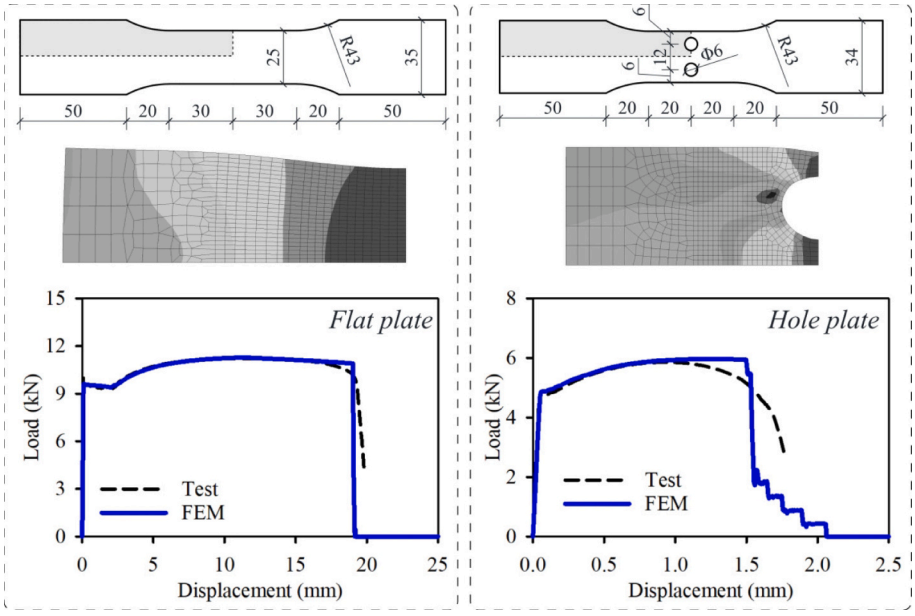

(b) Fracture calibration (unit: mm)

Fig. 7. Fracture calibration of steel deck.

2.3 times the clasped connection, respectively.

In summary, compared with the commonly used shear connection and clasped connection, the proposed folded connection and angle connection could significantly improve the efficiency of transferring the steel deck's in-plane tension and enhancing the deck connection's deformation capacity. When using the folded connection, it is recommended to use "tri-fold-2" type and apply the designed preload to the shear connectors. While using the angle connection, it is recommended to use "tri-fold" type configuration, and the preload applying to the bolts is not required.

4. RO modeling of prototype building

4.1. Frame

The RO model of the prototype building is illustrated in Fig. 9. The steel frame and floor slab were modeled by beam elements and shell elements, respectively. The connections between girders, beams and columns were modeled by spring elements, whereas properties of welds [63] were not considered. The contact between slab and steel frame was modeled by the "Automatic-General" contact. All the column bases were fully restrained. The blue dashed curve in Fig. 4 was used to model the material properties of floor beams and columns, while the load-deformation curve in Fig. 10 was used to model the axial behavior of connection springs. The connection's vertical shear load was assumed to be only resisted by the web bolts. According to [40], each bolt spring's shear capacity was calculated as 91 kN. The web bolt springs would be deleted when the axial fracture displacement (δ_0) or the vertical shear capacity was reached. The flange springs would only be removed when the axial displacement reached δ_0. The axial spring parameters (Fig. 10) were calibrated by corresponding HF models (Fig. 11), and the calibration procedure was identical to that discussed in Ref. [34]. In particular, the web spring parameters were first calibrated based on a HF model of the bolted web connection, which was extracted from the steel frame. The flange spring parameters were calibrated based on a HF half-span beam model (Fig. 11). Table 2 shows the calibrated spring parameters. Beam elements were used to model the bolted shear connectors, which failure was not modeled as a fully composite connection was designed between composite slabs and floor beams. Notably, according to the simulation results in Section 5, the maximum shear load achieved by the shear connectors was lower than its design shear resistance, so the simplification here was reasonable. It is worth noting that the corresponding HF modeling approach for the composite floor structures was validated in a previous study [56], which is reproduced in Appendix A, which may confirm the rationale of the calibrated RO models.

4.2. Composite slab

4.2.1. HF model

As shown in Fig. 12, an HF rebar-truss composite slab model was

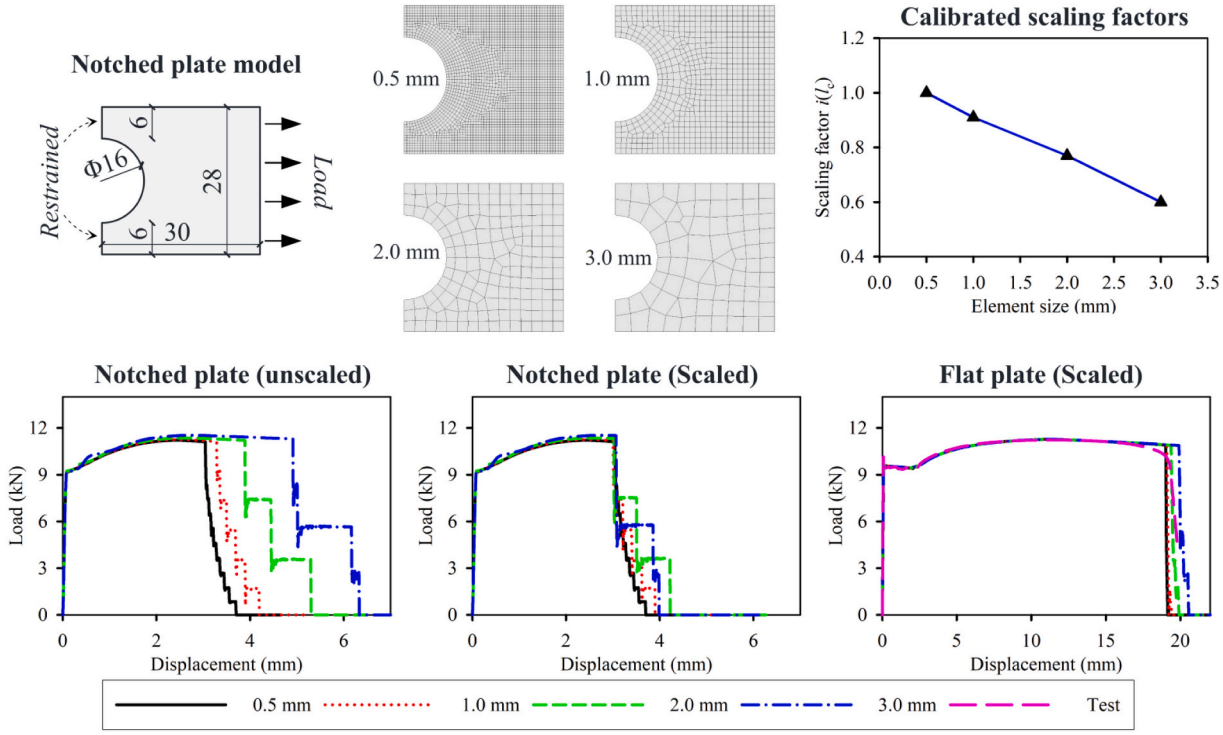

Fig. 8. Mesh-size regularization of steel deck fracture (unit: mm).

Table 1
Simulation results of deck connections.

Connection type		Preload (MPa)	R_u (kN)	δ_u (mm)	F_u (kN)	F_u / R_u
Shear connection		–	136.8	1.3	18.5	13.5%
Clasped connection		–		15.6	7.1	5.2%
Folded connection	half-fold	0		1.8	99.5	72.7%
	Tri-fold-1	0		1.8	102.1	74.6%
	Tri-fold-2	0		20.8	145.4	106.3%
	Tri-fold-2	300		29.6	159.9	116.9%
	Tri-fold-2	600		36.0	163.9	119.8%
Angle connection	half-fold	0		24.8	137.8	100.7%
	Tri-fold	0		36.0	151.0	110.4%
	Tri-fold	300		36.8	152.0	111.1%
	Tri-fold	600		34.8	149.2	109.1%
	Gate-fold-1	0		34.8	149.3	109.2%
	Gate-fold-2	0		36.5	147.3	107.7%

established based on a square slab (2.4 × 2.4 m) extracted from the prototype building. The HF model was taken as a benchmark for the later calibration of the corresponding RO slab model. Note that if it is assumed that the horizontal constraint from the neighboring structures was fully restrained under the progressive collapse scenario, the slab would be loaded in a tensile-bending stress state. Accordingly, this stress state was taken as the benchmark loading state to calibrate and validate RO slab models. By applying vertical loads to the slab's mid-span section and restraining its two parallel horizontal boundaries, the tensile-bending loading state could be simulated. For the HF slab model in Fig. 12, the loading states of bending about either the *y*-axis or the *x*-axis were taken into account.

The HF modeling method used and validated in Ref. [56] was

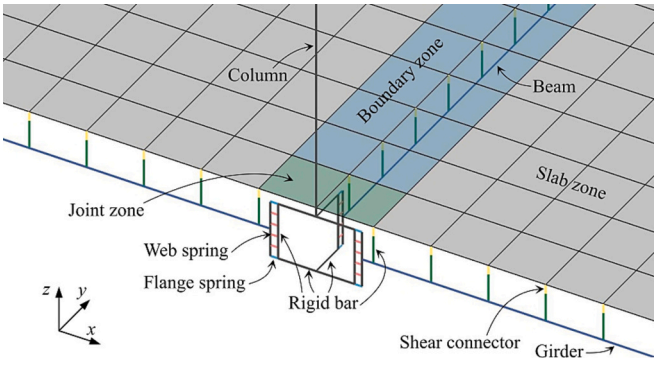

Fig. 9. RO model overview.

adopted in this section. In the HF slab model, the concrete slabs, bars and steel decks were modeled by solid, beam and shell elements, respectively. The bars were assumed to be perfectly integrated with the concrete and the relative sliding between them was ignored. The friction coefficient between steel decks and concrete slabs was taken as 0.5 [56]. The MAT100 material was used to model the spot weld between the steel deck and rebar-truss, which shear capacity was taken as 3 kN. The clasped connection between adjacent decks was modeled by a separated row of shell elements (Fig. 12). The MAT152 material was used to model the clasped connection's resistance along the y-axis direction, which equivalent stress-strain curve was shown in Fig. 12 and was derived from the corresponding simulation result (Fig. 5). The load-carrying capacity of the "clasped connection" shell element along the *x*-axis was ignored. The deformation of the nodes at the longitudinal boundaries parallel to the *x*-axis or *y*-axis was fully restrained, while the vertical loads were applied to the slab's mid-section (Fig. 12). As shown in Fig. 4, the concrete behavior was calibrated by the tests conducted by Sinha et al. [64] and Gopalaratnam and Shah [65]. The curves of the applied load versus the vertical displacement of the mid-section for the HF slab model in the case of bending about the *x*-axis or *y*-axis are shown

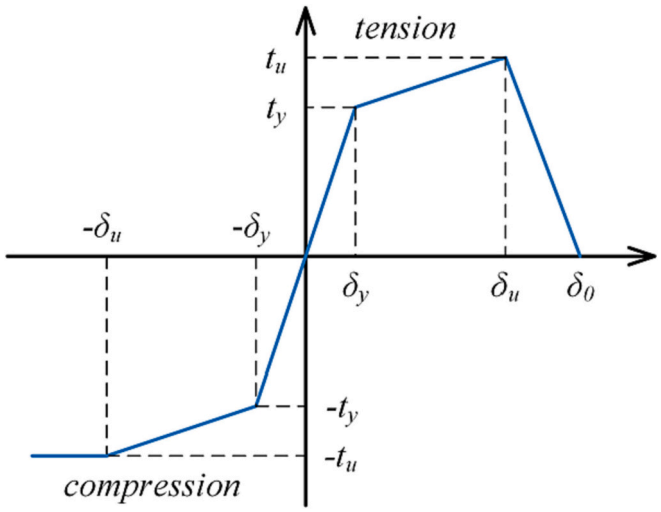

Fig. 10. Axial behavior of connection springs.

in Fig. 12.

4.2.2. Calibration of the RO model

In the RO model of the prototype building (Fig. 9), slabs were modeled by square shell elements with a side length of 300 mm. The "MAT_Concrete_EC2" material was used to model the material properties of steel deck, rebar, and concrete. The nonlinear behavior of concrete, rebars, or a combination of them could be simulated with this material by altering the reinforcement ratio. Meanwhile, these material properties were applied to the corresponding integration points in the shell elements.

The RO model of the rebar-truss composite slab had 12 integration points, including six concrete points, four rebar points, and two steel deck points (Fig. 13). The ratio between the rebar's cross-sectional area and its spacing was used to define the thickness of the corresponding rebar layer. The web bars of the rebar-trusses were neglected in the RO model. For the steel deck, it was assumed that its cracking in one direction would not affect its tensile strength in the orthogonal direction. Therefore, to avoid the interaction of the fracture behavior in the longitudinal and transverse directions, the steel deck behavior in these two directions was modeled by independent integration points. The steel deck's original thickness, 1.2 mm, was taken as the steel deck layer's thickness. The joint zone was modeled by four plain concrete layers (Figs. 9 and 13), which aimed to simulate the support from the column to the floor slabs under the sagging moment.

A square shell element with a side length of 300 mm was adopted as the benchmark model to calibrate the material properties of the concrete, rebar, and steel deck in the RO model (Fig. 13). The dimension of this benchmark model was identical to that used in the prototype building's RO model (Fig. 9) to maintain consistency. The stress-strain curves in Fig. 4 were initially adopted to define the material behavior of the steel deck and CRB550 rebar. Fig. 14 shows the corresponding simulation results, which were labeled as "scale 1". The numerical simulation results show that the simulated fracture displacement of the steel deck was larger than the test result. This is because the shell element size in the RO model was overly large to accurately capture the steel deck's local necking behavior, which was observed in the corresponding material coupon test. To tackle this issue, the steel deck's plastic strain value was reduced by multiplying a scaling factor. The scaling factor was calculated by dividing the fracture displacement of "scale 1" by the tested fracture displacement, which was equal to 0.85. After applying this scaling factor, the steel deck's simulation result could be consistent with the test result. The concrete behavior was simulated by the Mander model, and the confined ratio was 1.05 [66]. Thus, the concrete softening behavior under tension and compression was calibrated by the tests conducted by Gopalaratnam [65] and Sinha [64], respectively, and the results are shown in Fig. 14.

In accordance with the HF slab model in section 4.2.1, a RO slab model was also built for the square slab model (2.4 × 2.4 m) using 300 × 300 mm shell elements (Fig. 12). The bending performances of the RO

Table 2
Calibrated connection spring parameters.

	δ_y (mm)	t_y (kN)	δ_u (mm)	t_u (kN)	δ_0 (mm)
Flange spring	0.02	571	2	760	2.5
Bolt spring	1	125	13.5	160	16

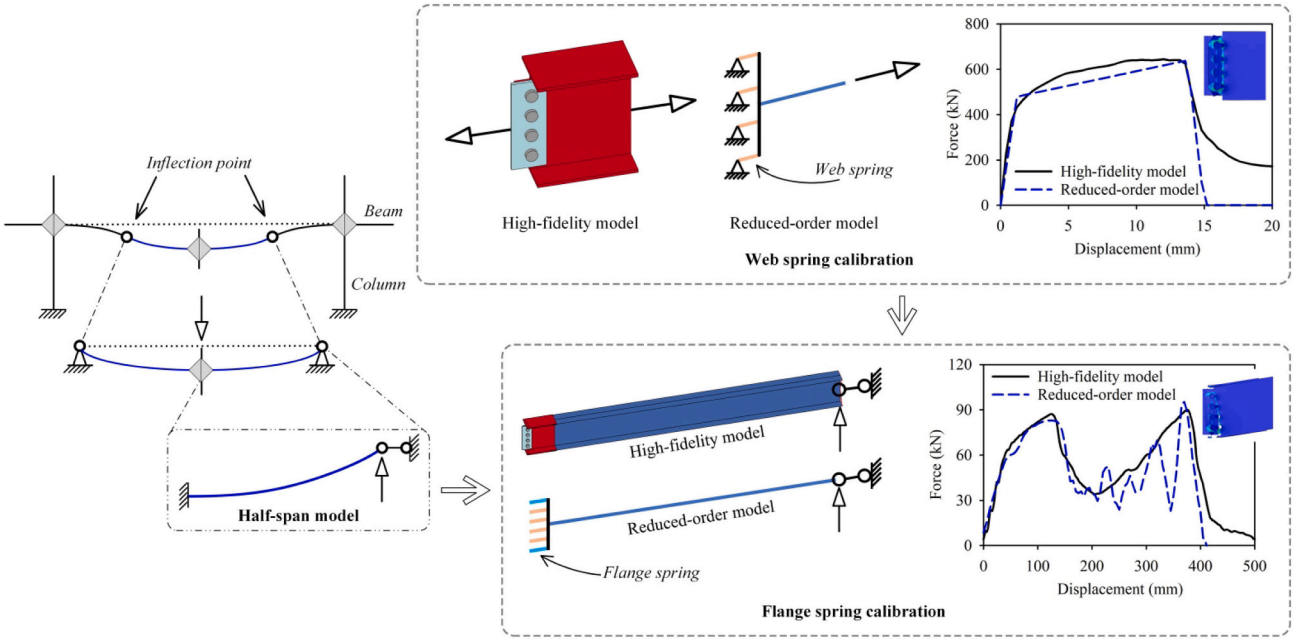

Fig. 11. Calibration of the spring parameters.

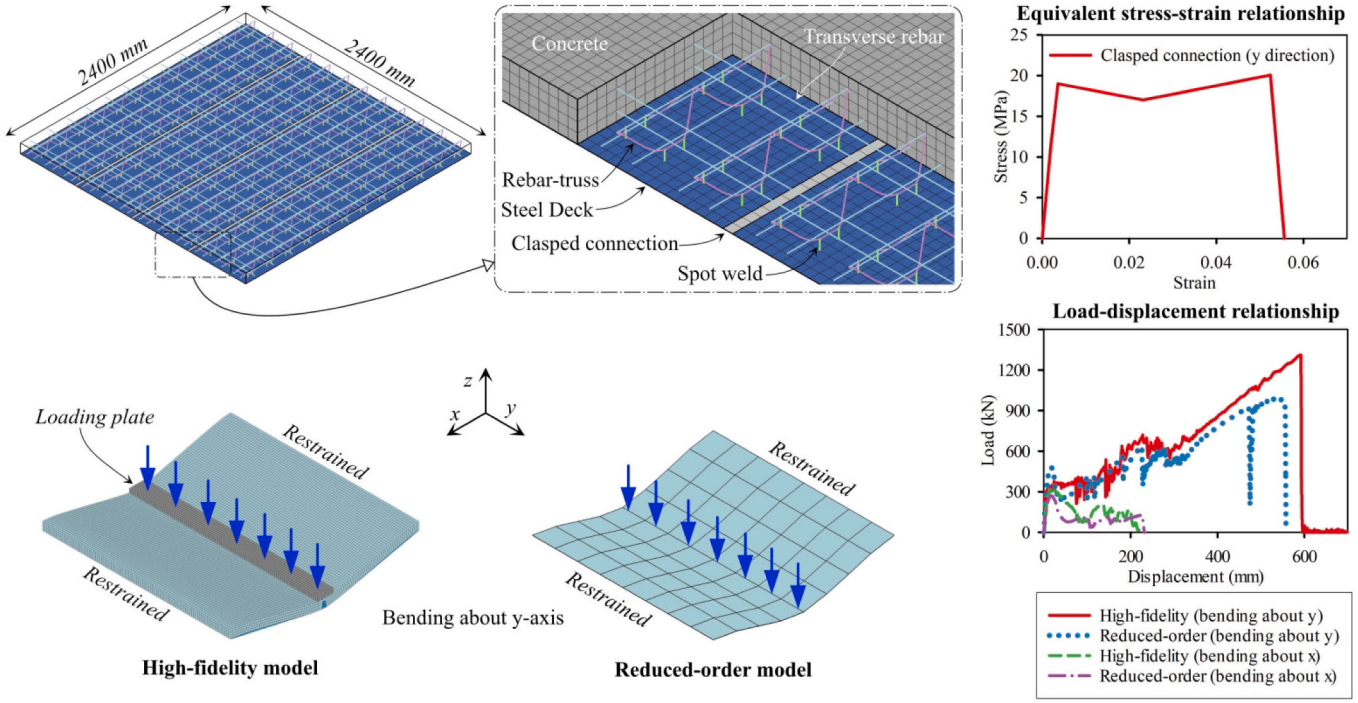

Fig. 12. HF benchmark model of rebar-truss composite slab.

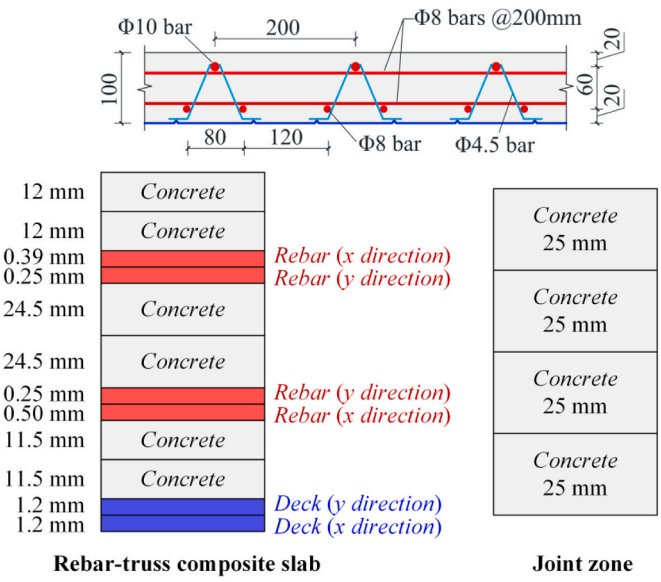

Fig. 13. RO modeling of floor slabs.

composite slabs about *y*-axis and *x*-axis were simulated using the calibrated material properties in Fig. 14. Fig. 12 compares the simulation results by the HF model and the RO slab model, and the adequacy the RO techniques for capturing the behavior of the composite slab is seen.

4.3. Deck connection

The RO modeling methods for the deck connections are described in this section. As shown in Fig. 9, except for the joint zone, the floor slab in the RO model of the prototype building was classified into two regions: slab zone and boundary zone. In the *x* direction, the calibrated steel deck's stress-strain relationship in Fig. 14 was applied to the corresponding steel deck integration point in the slab zone. In contrast, the steel deck integration point for the *x* direction in the boundary zone should be adjusted according to the structural behavior of the deck-to-beam connections, such as the shear connection and folded connection. All the steel deck integration point for the *y* direction in these two regions were adjusted according to the structural performance of the deck-to-deck connections, such as the clasped connection and angle connection. As shown in Fig. 12, the RO models of the deck connections were also calibrated based on the above-mentioned square shell element benchmark model, which size was 300 × 300 mm. Apart from the shear connection and clasped connection (Fig. 5), the "tri-fold-2" configuration with 600 MPa preload folded and the angle connection with "tri-fold" details without preload (Fig. 6) were also taken into account in this section.

An equivalent stress-strain curve was used in the RO shear connection model (Fig. 15). The stress in this equivalent curve was calculated by dividing the simulated structural resistance of the HF shear connection model by the steel deck's cross-sectional area (300 × 1.2 = 360 mm^2), while the equivalent strain was equal to the ratio between the simulated lateral deformation of the shear connection and the length of the RO model (300 mm). To facilitate the calibration, the equivalent curve for the shear connection was simplified to a perfectly plastic curve (Fig. 15) and the plastic value was determined by averaging the local maximum and local minimum values within the oscillation region. Similar to the RO calibration for the steel deck (Section 4.2), the simulated fracture displacement of the RO shear connection model using the unscaled equivalent stress-strain relationship "scale 1" was larger than the corresponding simulation result of the HF shear connection model. After applying a scaling factor of 0.93 to the equivalent strain, the numerically calculated curve of the RO shear connection model could match that of the HF model. A similar calibration method was also used for the RO models of the clasped connection, folded connection, and angle connection. As shown in Fig. 15, similar with the clasped connection, both the equivalent strain for the folded connection and angle connection should also be scaled by 0.93.

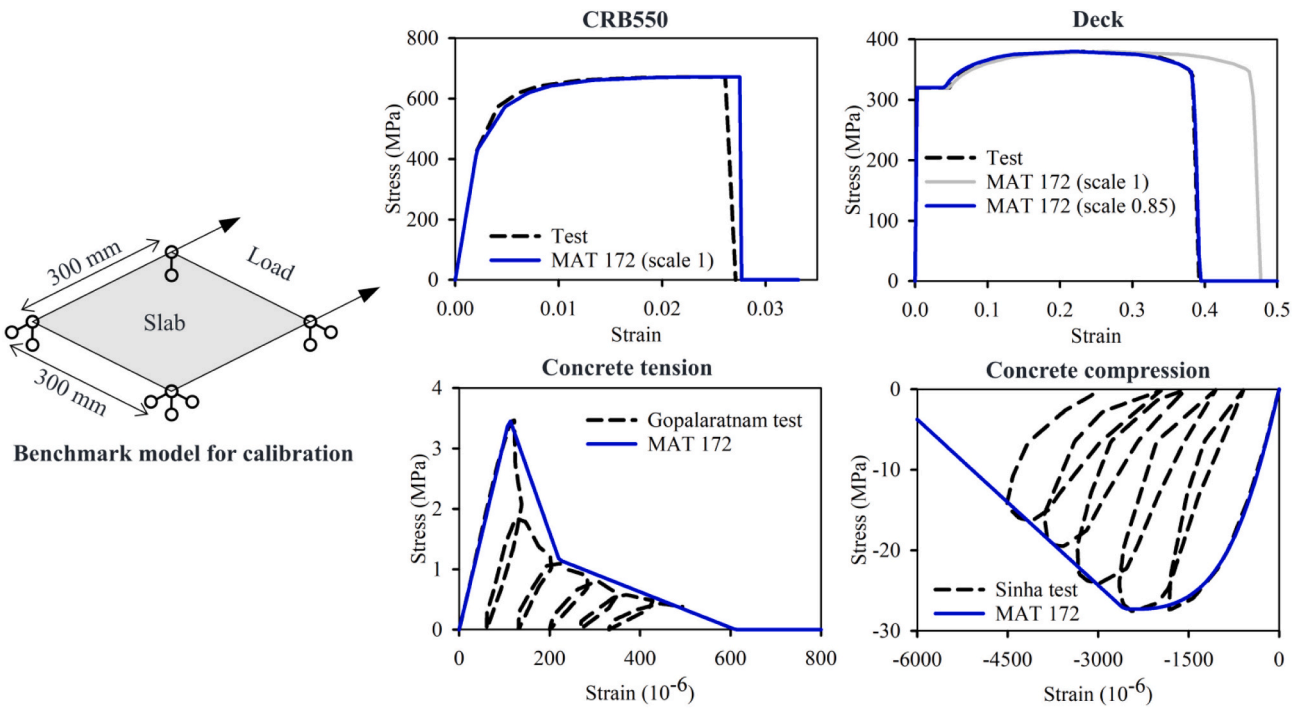

Fig. 14. Material calibrations for the RO slab model.

4.4. Loading method

Considering the symmetrical structural layout, there were nine single-column removal scenarios on the ground floor (Fig. 16a), which were represented by A5, A4, A3, B5, B4, B3, C5, C4, and C3, respectively. For each column removal scenario, the prototype building was loaded using a two-phase pseudo-static approach, which was proposed by Bao et al. [67]. In the 1st phase, a service level gravity load, R_d, was applied uniformly to all floor slabs. The R_d for the prototype building was 7 kN/m^2, which was derived from the load combination for extraordinary events in ASCE/SEI 7–16 [68], 1.2DL + 0.5LL. Then, in the 2nd phase, an extra monotonically increasing load was applied uniformly to the removed column's "directly affected bays" until the building collapsed. Besides, a rigid wall was built at the column base level to model the ground, and all the falling structural components would fall on this rigid wall (Fig. 16b).

For the "directly affected bays" under each column failure scenario, the floor load intensity, ω, could be derived from the reaction forces at the directly affected columns' bases. It is worth noting that the reaction forces at these column bases included the floor loadings of the "directly affected bays" and the "additional tributary area". As shown in Fig. 16, the "additional tributary area" was the floor area within the half-span girder length area beyond the "directly affected bays". Given this, Eqs. (1) and (2) was used to calculated ω.

$$\omega = \begin{cases} \dfrac{\lambda F_c}{nA_a}, & 1^{st}phase \\ \dfrac{F_c}{nA_a} - \dfrac{(1-\lambda)F_c{}'}{nA_a}, & 2^{nd}phase \end{cases} \quad (1)$$

$$\lambda = \frac{A_a}{A_a + A_t} \quad (2)$$

In the above equations, F_c was the vertical component of the total reaction force at the directly affected columns' bases; n was equal to the 5, representing the total number of floors; A_a and A_t represented the area of the directly affected bays and additional tributary area of each floor, respectively; F'_c was equal to the F_c at the dividing point between 1st phase and 2nd phase. In Fig. 16, l_B and l_G were represented the span length of beam and girder, respectively. For each column failure scenario, the corresponding A_a, A_t, and λ are listed in Table 3.

5. Analysis and discussion

5.1. Load-displacement curves

Using the RO modeling approach, the static curves between the load intensity and the vertical displacement at the removed column were obtained (Fig. 17). The static ultimate resistance, F_{su}, and corresponding vertical displacement at the removed column, δ_{su}, are summarized in Table 4, and the corresponding peak load points (δ_{su}, F_{su}) are also marked in Fig. 17. In this section, the prototype building with the shear connection and the clasped connection was represented by the "Common practice", while that with the "tri-fold-2" configuration and 600 MPa preload and the "tri-fold" angle connection without preload was named as "Enhanced".

According to Table 4, compared with the "Common practice" case, the F_{su} of the "Enhanced" case under each column removal scenario was improved. For the interior column removal scenarios (B4, B3, C4, C3), the improvement percentage of F_{su} ranged from 19% ~ 30%, while for the exterior column removal scenarios (A5, A4, A3, B5, C5), the corresponding percentage range was between 6% ~ 14%. This is because the improved in-plane tensile membrane action by the enhanced deck connections was more effective for the interior column removal scenarios, as the two-way load-carrying capacity could be fully developed by the slab reinforcements and steel decks. For the exterior column removal scenarios of the "Enhanced" case, even though the F_{su} was not significantly improved compared with the interior column removal scenarios, the structural resistance after the peak load points was also significantly enhanced owing to the improved in-plane tensile membrane action (Fig. 17). Overall, compared with the "Common practice" case, the minimum F_{su} of the "Enhanced" case was been improved by 17.18%. For the "Common practice" case, the minimum F_{su} was achieved by the B4 scenario; however, as the interior column removal scenarios' structural resistance was significantly enhanced, the

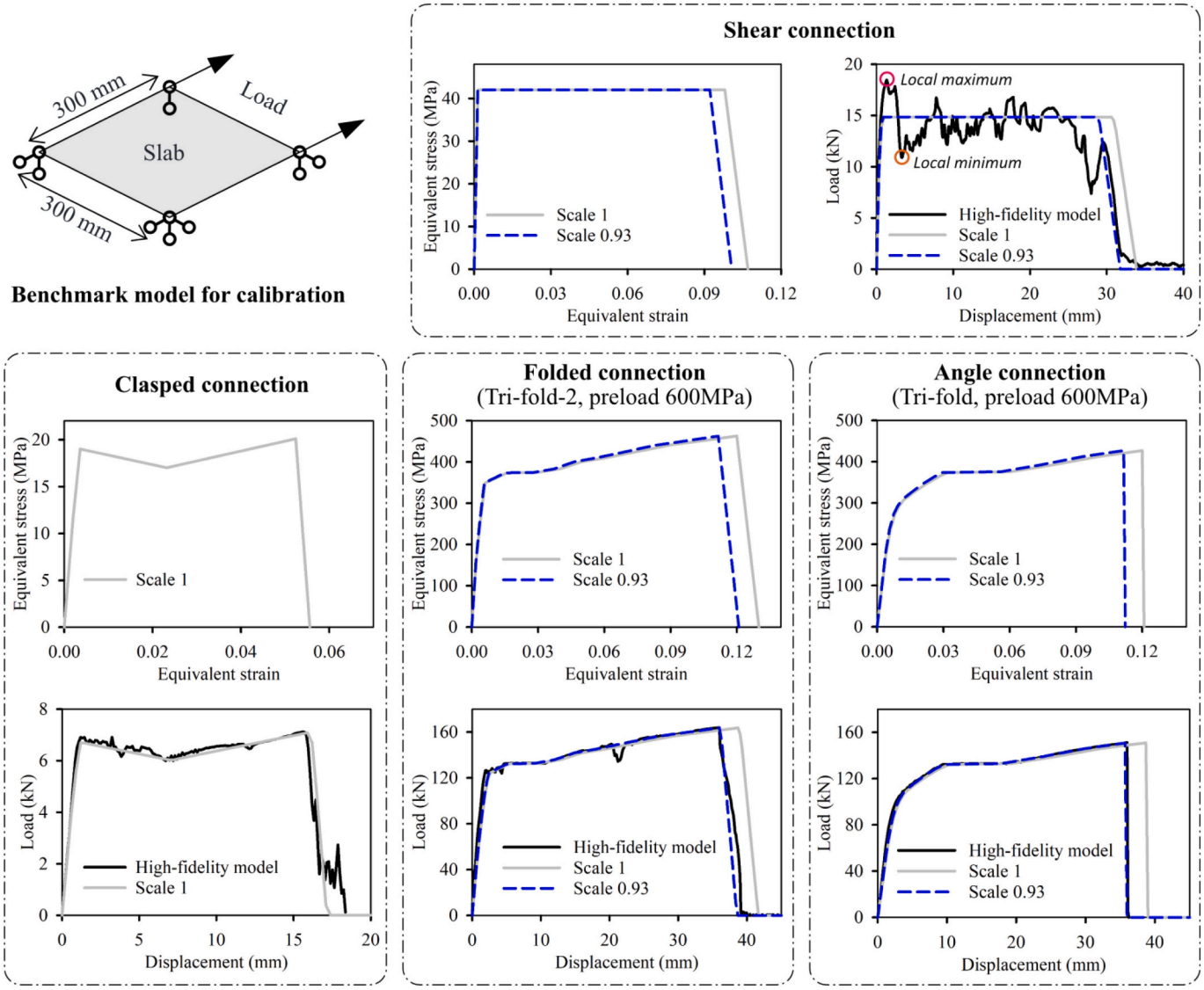

Fig. 15. RO calibration for the deck connections.

minimum F_{su} of the "Enhanced" case was found in the A4 scenario.

As shown in Fig. 17, in the "Enhanced" case, the most profound improvement of the F_{su} was found in the C4 scenario, in which the improvement percentage was 30%. Although the C3 scenario had the highest F_{su}, its improvement ratio of 26% was lower than that of the C4 scenario. Moreover, as shown in Fig. 17, when the F_{su} (44.05 kN/m^2) was achieved, the resistance of the C3 scenario was suddenly dropped to about 30 kN/m^2, while the resistance of the C4 scenario could maintain the load-carrying capacity at a level similar to the F_{su} (42.09 kN/m^2) until the collapse was triggered. This difference could be explained by the failure modes shown in Fig. 18.

For the C4 scenario, the structural collapse in the "Enhanced" case was spread to the entire building, while the structural collapse in the "Common practice" case was only developed within the directly affected bays. This is because the enhanced deck connections significantly enhanced the continuity between neighboring slabs, and the falling slabs in the directly affected bays would pull the neighboring slab down progressively, resulting in the entire building collapse. In this situation, as shown in Fig. 18, the horizontal boundary constraint was relatively weaker than the floor's in-plane tension, and the neighboring bays in the x direction were pulled horizontally towards the directly affected bays. While for the "Common practice" case, the horizontal boundary constraint was relatively stronger than the floor's in-plane tension, which caused the structural collapse to be limited within the directly affected bays. As noted by Wang et al. [22], a strong horizontal constraint would result in the connections and slabs fractured earlier than that with a relatively weaker horizontal constraint, which would also limit the development of the load-carrying capacity in the large deformation state ($\geq 0.1 l_G$). As listed in Table 4, the δ_{su} of the C4 scenario in "Enhanced" was 2177 mm, which was about five times that of the "Common practice".

For the C3 scenario, attributed to the surrounding frames, the horizontal boundary constraint was much stronger than that of the C4 scenario and was also stronger than the floor's in-plane tension in both "Common practice" and "Enhanced" cases. Consequently, for the C3 scenario in the "Enhanced" case, the structural collapse was not spread to the entire building, and the δ_{su} were also much smaller than that of the C4 scenario. Moreover, in the "Enhanced" case, the load-carrying capacity of the C3 scenario in the large deformation stage was also smaller than that of the C4 scenario.

5.2. Dynamic effect

The analysis in Section 5.1 was performed in a static approach and

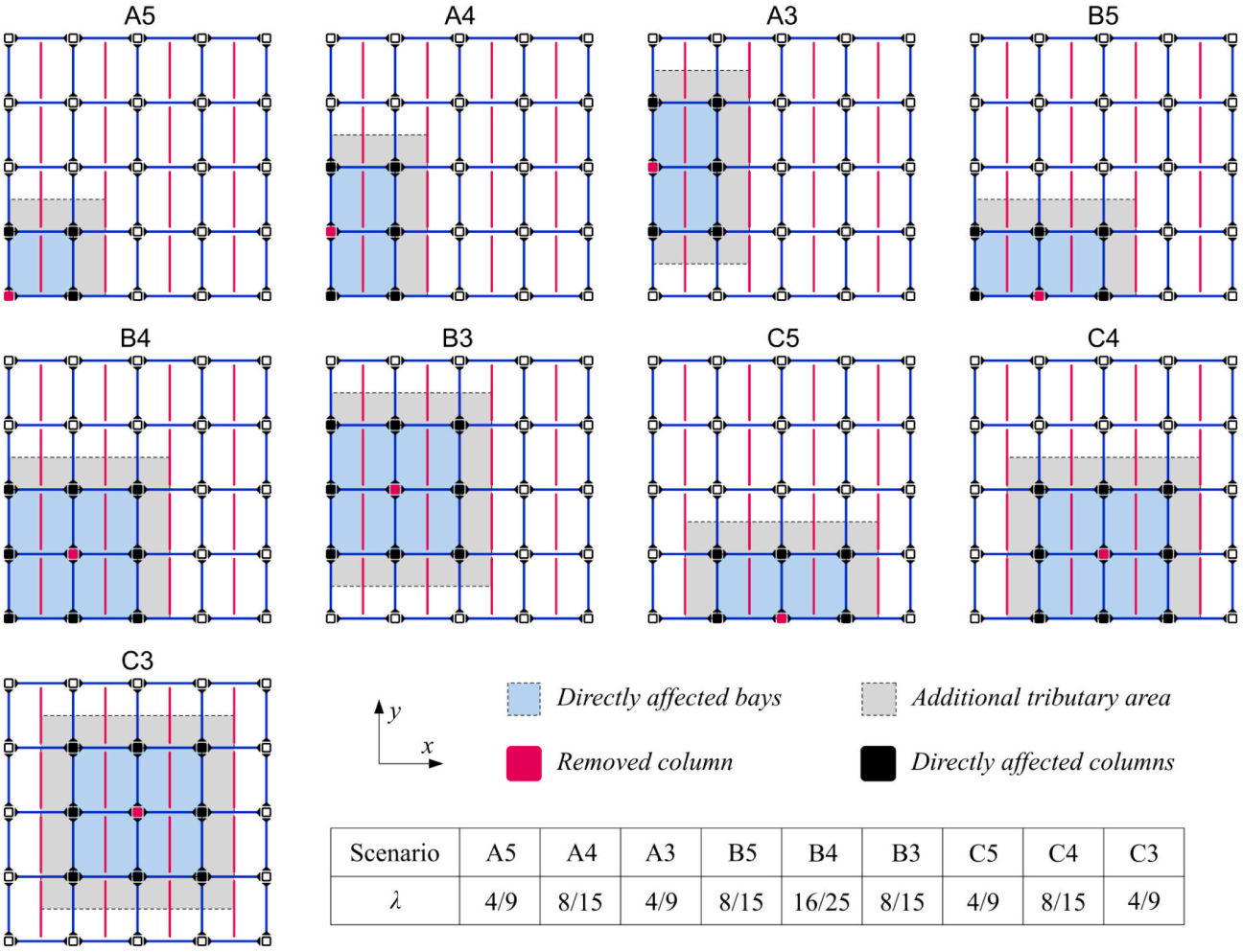

Scenario	A5	A4	A3	B5	B4	B3	C5	C4	C3
λ	4/9	8/15	4/9	8/15	16/25	8/15	4/9	8/15	4/9

(a) Floor area for calculating load intensity under each column failure scenario.

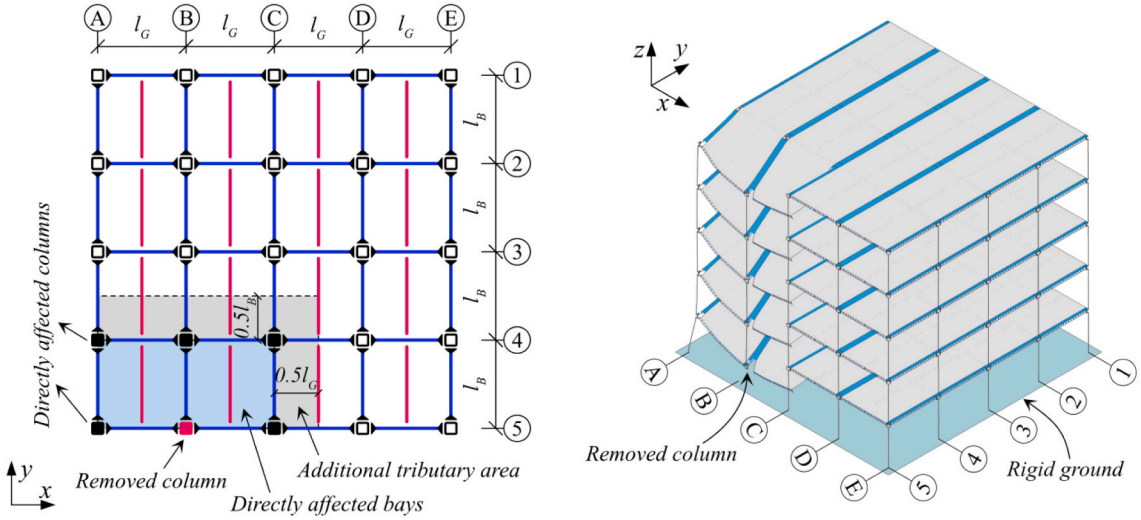

(b) Analysis of the prototype building under B5 column failure scenario

Fig. 16. Loading method for the prototype building.

Table 3
A_a, A_t, and λ of each column failure scenario.

Column loss location	A5	A4	A3	B5	B4	B3	C5	C4	C3
A_a	$l_G l_B$	$2l_G l_B$	$2l_G l_B$	$2l_G l_B$	$4l_G l_B$	$4l_G l_B$	$2l_G l_B$	$4l_G l_B$	$4l_G l_B$
A_t	$5l_G l_B/4$	$7l_G l_B/4$	$5l_G l_B/2$	$7l_G l_B/4$	$9l_G l_B/4$	$7l_G l_B/2$	$5l_G l_B/2$	$7l_G l_B/2$	$5l_G l_B$
λ	4/9	8/15	4/9	8/15	16/25	8/15	4/9	8/15	4/9

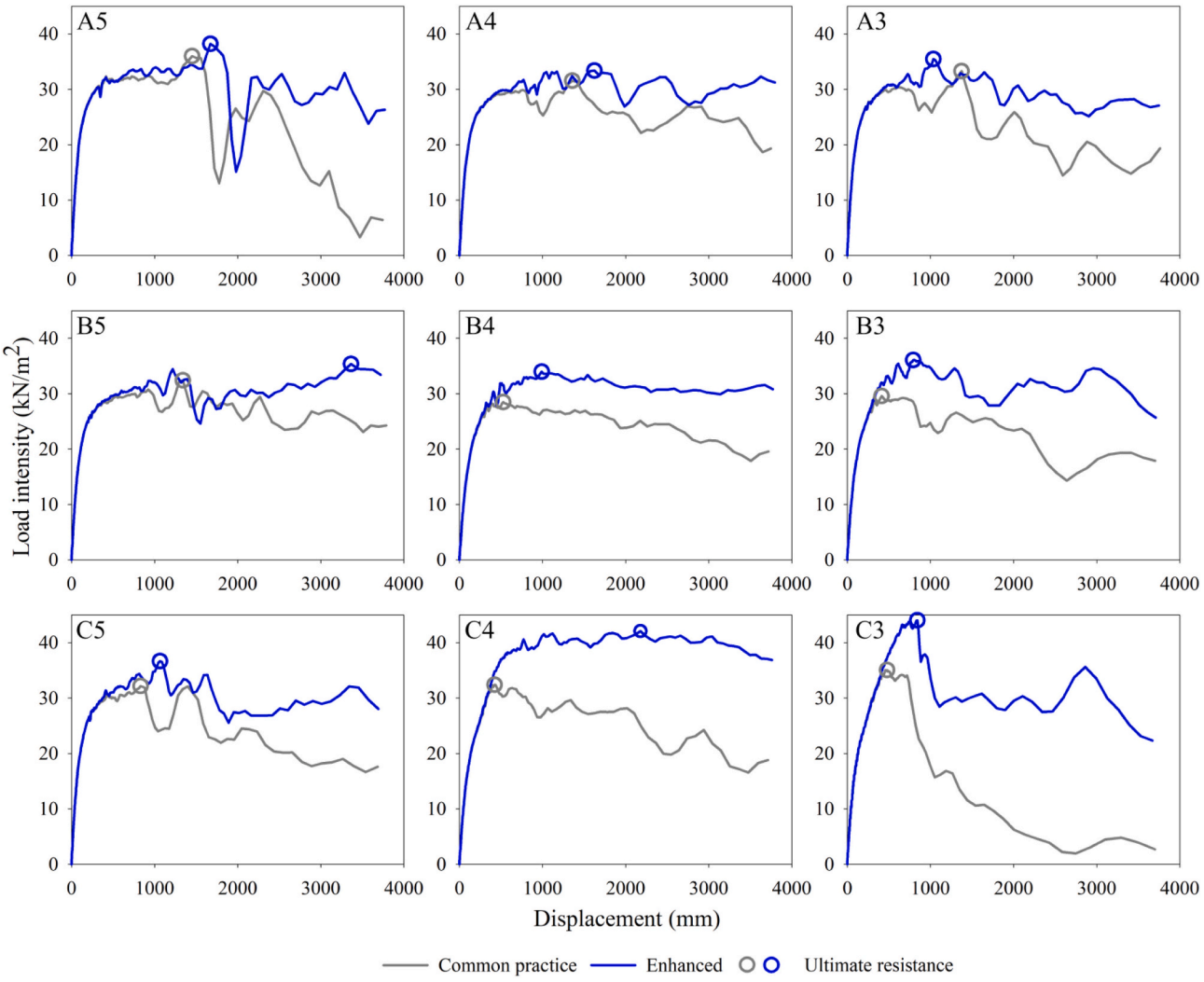

Fig. 17. Static load intensity - displacement curves of prototype building.

would not truly represent the structural behavior of the prototype building in the dynamic collapse situation. Given this, an energy-based method was used to transform the nonlinear static response into the equivalent dynamic response (Fig. 19a), which was proposed by Izzuddin et al. [69]. After reaching F_{su}, the structure would become unstable and might suddenly collapse [67]. Hence, the static curve after F_{su} was neglected when calculating the equivalent dynamic response curve. The peak of the equivalent dynamic response curve could be considered as the dynamic ultimate capacity (F_{du}) of the structure against progressive collapse under this scenario. The minimum F_{du} in all column removal scenarios could be considered as the ultimate capacity of the objective structure. The demand for the progressive collapse resistance of this structure could be represented by R_d. The structural robustness index, Ω, could be expressed as the ratio of "minimum F_{du}" to "R_d". If Ω was >1, the structure would be strong enough to prevent progressive collapse. If not, the structure should be redesigned until its Ω was >1. The corresponding F_{du} of the static analysis results were shown in Fig. 19b and Table 4.

According to Table 4, for the "Common practice" case, the F_{du} of exterior column removal scenarios (26.81–30.01 kN/m^2) were all higher than that of the interior column removal scenarios (21.59–24.55 kN/m^2). This is because, in the interior column removal scenario, the tributary floor area of the girders and beams connected to the removed column was smaller than that of the exterior column removal scenario, and this phenomenon was also noted in Ref [23]. Hence, under the sudden column removal situation, the interior column removal scenarios were more vulnerable than the exterior column failure scenarios. However, after equipping with the enhanced deck connection, attributed to the enhanced two-way load-carrying capacity of the floor slab, the F_{du} of the interior column failure scenarios was significantly improved with a percentage range of 22% ~ 64%, which was much higher than that of the exterior column removal scenarios (6% ~ 10%). As a result, although the F_{du} of the exterior column failure scenarios was not improved significantly, the Ω of the "Enhanced" case (390%) was

Table 4
F_{su} and F_{du} of prototype building.

Column loss location	Common practice			Retrofitted		
	δ_{su}	F_{su}	F_{du}	δ_{su}	F_{su}	F_{du}
A5	1450	36.01	30.01	1671	38.20	31.12
A4	1357	31.55	26.81	1623	33.38	28.96
A3	1375	33.28	27.39	1035	35.46	28.22
B5	1338	32.41	27.15	3362	35.36	29.74
B4	526	28.49	22.32	989	33.97	27.32
B3	413	29.58	21.59	794	36.08	27.62
C5	831	32.16	26.92	1065	36.66	29.21
C4	422	32.40	22.40	2177	42.09	36.66
C3	478	35.07	24.55	843	44.05	32.13
Min		28.49	21.59		33.38	27.32
Max		36.01	30.01		44.05	36.66
Min F_{du} /R_d (Ω)			308%			390%

* Notes: the unit of F_{su} and F_{du} in this table is kN/m^2, and the unit of δ_{su} in this table is mm.

already 27% higher than that of the "Common practice" case (308%). In conclusion, for the prototype building with the commonly used deck connections, the proposed enhanced deck connections could effectively improve its structural robustness.

As shown in Fig. 19b and Table 4, after using the enhanced deck connections, the C4 scenario had the highest improvement percentage of F_{du}, 64%, while that of the other interior column failure scenarios fell in the range of 22% ~ 31%. The significant improvement of F_{du} under the C4 scenario was attributed to the horizontal deformation of the neighboring bays towards the directly affected bays (Fig. 18), postponing the failure of the connections and slabs. However, this exaggerated enhancement of the F_{du} would be detrimental, as it would trigger the structural collapse to spread to the entire building. When applying the enhanced deck connections to large size buildings with a lot of bays, it is recommended to horizontally divide the entire buildings into several zones, and the bays located in these zones' boundaries would use relatively weaker deck connections. For these boundary bays, their floor's in-plane tensile capacity must be designed to be insufficient to spread the structural collapse to their surrounding bays, and they also need to be robust enough to resist the incidental loads caused by the column failure within these bays. By using this method, the local structural collapse would not likely be spread to the entire building.

5.3. Limitations

Although the numerical models presented in this study were very detailed, it should be noted that there were several limitations when compared to the actual building configurations. In addition, the enhanced deck connections might have an impact on the construction speed and cost.

1. Even if the angles used in the angle connection were designed to improve the tensile capacity of the steel decks in the y direction, they would also contribute to the floor slab's bending resistance about the y-axis and tensile strength in the x direction to some extent. Hence, the reduced-order analysis results in Section 5 might undervalue the actual progressive collapse resistance of the "Enhanced" prototype building.
2. In this study, the RO models were calibrated by the corresponding HF models. The efficiency of the HF modeling approach for the composite floor system was validated in a previous study [56] (Appendix A). As pointed out in [56], the fracture behavior of steel structures under the progressive collapse scenarios could be accurately simulated by the steel fracture models that were carefully calibrated by the detailed coupon test results. As for the steel deck connections proposed in this study, although the steel deck fracture model used in

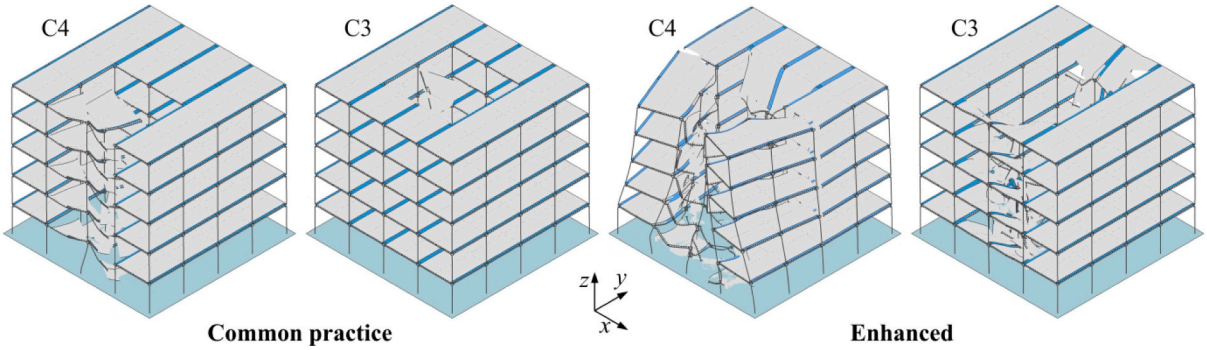

Fig. 18. Failure modes of the C4 and C3 scenarios.

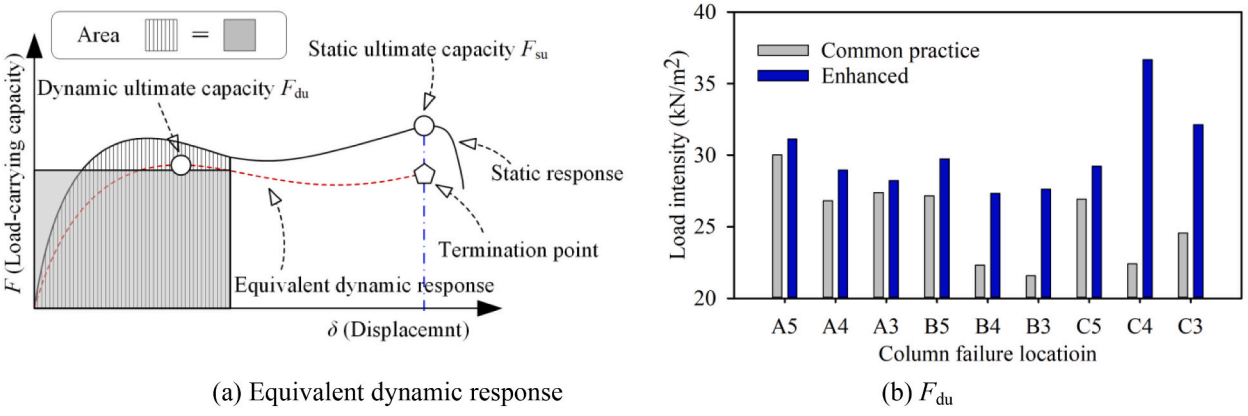

(a) Equivalent dynamic response (b) F_{du}

Fig. 19. Structural dynamic response.

the corresponding HF deck connection models was precisely calibrated, the simulation results of the HF models were not directly validated by the experimental test results, which would limit the efficiency of these HF models. In addition, there is test evidence that the friction coefficients of steel may vary [22,59,60,70,71,72], and hence these HF deck connection models would need to be recalibrated and adjusted when corresponding experimental test results are available in future. The localized failure such as buckle of steel tubes or plates [73] was also excluded from the RO model. The results were obtained based on a typical codified steel frame, and hence the research findings may not apply to novel systems such as high strength steel frame structures [74–77] as the behavior of high strength steel [78–84] is different from normal steels.

3. The enhanced deck connections designed in this paper were based on the bolted shear connector, which was mainly used to improve the sustainability and deconstructablity of the structures. Even if this is a trend to improve the recyclability of the buildings, the welded shear studs are still widely used in the current construction of steel frame buildings with composite slabs to expedite the construction speed. However, when it is necessary to improve the progressive collapse resistance of a steel frame building by enhancing the deck-to-beam connection's strength, the engineer can refer to the design ideas in this paper and design similar enhanced deck connections for that using welded shear studs.
4. Although these enhanced deck connections can effectively improve structural robustness, they could also lead to more material consumption and increase construction complexity, thus increasing construction costs and slowing down construction speed. Generally, the typical width of the rebar-truss steel deck was equal to or slightly $<$600 mm [44]. When using the enhanced deck connections, this narrow deck width would lead to a large amount of angle usage. Therefore, the authors suggest that when using the angle connections proposed in this paper, it is recommended to use the steel decks with larger widths as far as possible to increase the spacing of the angle connection, and thus reduce the amount of angle used. As shown in Fig. 2, the deck width in the composite floor with enhanced connections was chosen to be 1 m. In addition, compared with the enhanced deck connections, it might be a more economical and simpler way to improve the structural robustness of steel frame buildings by designing more rebars or using rebars with higher strength and ductility. However, these enhanced deck connections also provide another way to improve the structural robustness of steel frame buildings.
5. As noted in section 5.2, the Ω of the "common practice" case was 3.08, which was already robust enough to resist progressive collapse caused by the failure of a single ground floor column. This is because, according to the Chinese code, the composite action between the composite slabs and steel beams was not considered in the seismic elastic-plastic analysis, i.e., the potential contribution of the composite slab in resisting the seismic-induced bending moment was ignored. Therefore, this simplifying assumption in the current specification led to this relatively conservative design. This echoes the findings in [34], where the composite slab more than doubled the structural robustness of a steel frame building. It also echoes the existing test results of the composite floor system, when the beam-to-column connections were rigid joint, the progressive collapse resistance under the single column failure scenarios was very likely to far exceed the design requirements [11,13,14,18]; while when the hinged beam-to-column connections were used, the corresponding progressive collapse resistance of the composite floor might be insufficient [10]. Given this, applying these enhanced deck connections to the steel frames with hinged beam-to-column connections might have a more significant effect on improving the structural robustness.

6. Conclusions

To improve the performance of the profiled steel decks under progressive collapse scenario, this study proposed two novel types of enhanced deck connections for improving the load-carrying capacity of the deck-to-beam connection and deck-to-deck connection. First, the structural performance of the designed deck connections in transferring steel decks' in-plane tensile load was numerically investigated and compared based on HF deck connection models. Then, using carefully calibrated RO models, the effect of the enhanced deck connections on improving the progressive collapse resistance of steel frame structures was investigated based on a five-story prototype building. Based on the analysis results in this study, the following conclusions were reached:

1. The HF analysis results of the deck connections showed that the ultimate resistance of the shear connection and clasped connection designed for the prototype building only reached 13.5% and 5.2% of the steel deck's sectional tensile capacity, respectively, which would limit the development of the tensile membrane action of the profiled steel decks under the progressive collapse scenario.
2. The folded connection was designed to replace the shear connection to improve the deck-to-beam connection's strength. The "tri-fold-2" configuration was recommended for the folded connection, which was realized by folding the steel deck twice and restraining the free deck edges by the bolts. Its load-carrying capacity increased with preload applied to the bolted shear connector. After applying with 600 MPa preload, based on the HF analysis results, the ultimate resistance and corresponding deformation capacity of the "tri-fold-2" folded connection were 8.9 and 20.2 times the shear connection, respectively.
3. The tri-fold configuration was recommended for the angle connection, and its load-carrying capacity was not significantly affected by the bolt preload. Based on the HF analysis results, the ultimate resistance and corresponding deformation capacity of the tri-fold angle connection without preload were 20.3 and 2.3 times the clasped connection, respectively.
4. According to the RO analysis results, the structural robustness of the prototype building with enhanced deck connections ("tri-fold-2" folded connection and "tri-fold" angle connection) was 27% higher than that with the commonly used deck connections.
5. After replacing the commonly used deck connections with the enhanced deck connections, the dynamic ultimate resistance of the interior column removal scenarios and exterior column removal scenarios was improved with a percentage range of 22% $\sim$ 64% and 6% $\sim$ 10%, respectively. Attributed to the enhanced two-way load-carrying capacity of the floor slab, the dynamic ultimate resistance of the interior column removal scenarios was improved more significantly than that of the exterior column removal scenarios.

CRediT authorship contribution statement

Junjie Wang: Conceptualization, Methodology, Investigation, Writing – original draft. **Ke Ke:** Software, Writing – review & editing, Supervision, Resources, Funding acquisition. **Michael C.H. Yam:** Supervision, Resources, Funding acquisition, Writing – review & editing. **Minghong Teng:** Writing – review & editing. **Wei Wang:** Resources, Supervision, Writing – review & editing.

Declaration of Competing Interest

There is no financial/personal interest or belief that could affect our objectivity. There are no potential conflicts of interest either.

Data availability

Data will be made available on request.

Acknowledgments

The research work in this paper was sponsored by the Natural Science Foundation of China (No 52178111 and 51820105013) and Chinese National Engineering Research Centre for Steel Construction, The Hong Kong Polytechnic University (Project No. BBVW). The funding support provided by the Fundamental Research Funds for the Central Universities 2022CDJQY-009 is also acknowledged.

Appendix A. Appendix

The feasibility of the HF modeling approach to simulate the progressive collapse behavior of steel frame buildings with composite slabs can be verified using a full-scale test on a composite floor structures, which corresponding HF model is illustrated in Fig. A1a. Fig. A1b shows the comparison of the vertical resistance versus vertical displacement at the removed column curves between the experimental result and simulated result. The reader interested in more details about the experimental program and modeling techniques may refer to [56].

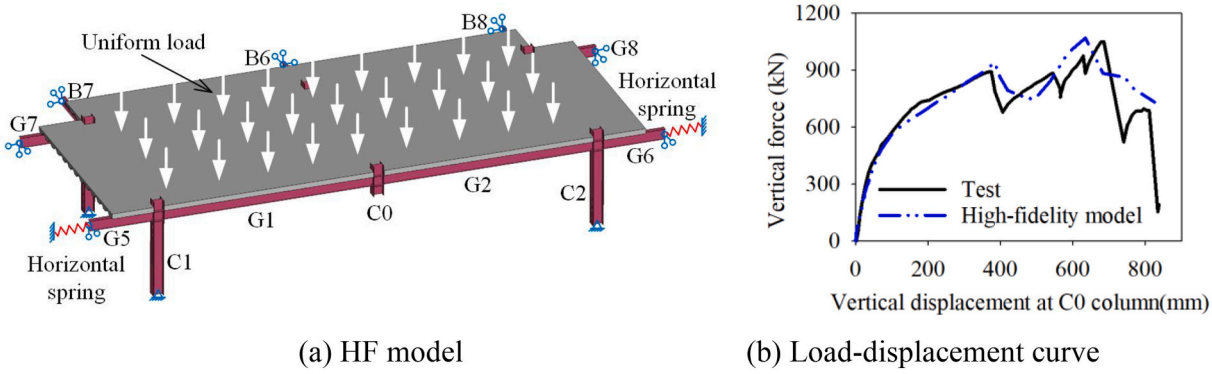

Fig. A1. Validation of HF composite floor model [56].

References

[1] Y. Chen, K. Ke, Seismic performance of high-strength-steel frame equipped with sacrificial beams of non-compact sections in energy dissipation bays, Thin-Walled Struct. 139 (2019) 169–185.
[2] K. Ke, M.C.H. Yam, P. Zhang, Y. Shi, Y. Li, S. Liu, Self-centring damper with multi-energy-dissipation mechanisms: insights and structural seismic demand perspective, J. Constr. Steel Res. (2023) 107837, https://doi.org/10.1016/j.jcsr.2023.107837.
[3] H. Zhang, X. Zhou, K. Ke, M.C.H. Yam, X. He, H. Li, Self-centring hybrid-steel-frames employing energy dissipation sequences: Insights and inelastic seismic demand model, J. Build. Eng. (2023) 105451.
[4] X. Zhou, Y. Huang, K. Ke, M.C.H. Yam, H. Zhang, H. Fang, Large-size shape memory alloy plates subjected to cyclic tension: towards novel self-centring connections in steel frames, Thin-Walled Struct. (2023), 110591, https://doi.org/10.1016/j.tws.2023.110591.
[5] Z.Y. Zhou, Y.Y. Chen, M.C.H. Yam, K. Ke, X.Z. He, Experimental investigation of a high strength steel frame with curved knee braces subjected to extreme earthquakes, Thin-Walled Struct. (2023), 110596, https://doi.org/10.1016/j.tws.2023.110596.
[6] B. Yang, K.H. Tan, Behavior of composite beam-column joints in a middle-column-removal scenario: Experimental tests, J. Struct. Eng. 140 (2014) 04013045.
[7] B. Yang, K.H. Tan, G. Xiong, Behaviour of composite beam–column joints under a middle-column-removal scenario: component-based modelling, J. Constr. Steel Res. 104 (2015) 137–154.
[8] W. Wang, J. Wang, X. Sun, Y. Bao, Slab effect of composite subassemblies under a column removal scenario, J. Constr. Steel Res. 129 (2017) 141–155.
[9] J. Wang, W. Wang, D. Lehman, C. Roeder, Effects of different steel-concrete composite slabs on rigid steel beam-column connection under a column removal scenario, J. Constr. Steel Res. 153 (2019) 55–70.
[10] E.S. Johnson, J.E. Meissner, L.A. Fahnestock, Experimental behavior of a half-scale steel concrete composite floor system subjected to column removal scenarios, J. Struct. Eng. 142 (2015) 04015133.
[11] Q.N. Fu, K.H. Tan, X.H. Zhou, B. Yang, Load-resisting mechanisms of 3D composite floor systems under internal column-removal scenario, Eng. Struct. 148 (2017) 357–372.
[12] M. Hadjioannou, S. Donahue, E.B. Williamson, M.D. Engelhardt, Large-scale experimental tests of composite steel floor systems subjected to column loss scenarios, J. Struct. Eng. 144 (2018) 04017184.
[13] Q.N. Fu, K.H. Tan, X.H. Zhou, B. Yang, Three-dimensional composite floor systems under column-removal scenarios, J. Struct. Eng. 144 (2018) 04018196.
[14] J. Wang, W. Wang, Y. Bao, D. Lehman, Full-scale test of a steel moment-resisting frame with composite floor under a penultimate edge column removal scenario, J. Constr. Steel Res. 162 (2019), 105717.
[15] R. Zandonini, N. Baldassino, F. Freddi, G. Roverso, Steel-concrete frames under the column loss scenario: an experimental study, J. Constr. Steel Res. 162 (2019), 105527.
[16] L.M. Ren, B. Yang, K. Chen, Y.J. Sun, D.Y. Kong, Progressive collapse of 3D composite floor systems with rigid connections under external column removal scenarios, J. Struct. Eng. 146 (2020) 04020244.
[17] J.Z. Zhang, G.Q. Li, J. Jiang, Collapse of steel-concrete composite frame under edge-column loss—experiment and its analysis, Eng. Struct. 209 (2020), 109951.
[18] J. Wang, W. Wang, Y. Bao, Full-scale test of a steel–concrete composite floor system with moment-resisting connections under a middle-edge column removal scenario, J. Struct. Eng. 146 (2020) 04020067.
[19] L. Guo, S. Gao, Y. Wang, S. Zhang, Tests of rigid composite joints subjected to bending moment combined with tension, J. Constr. Steel Res. 95 (2014) 44–55.
[20] X. He, K. Ke, L. Guo, M.C.H. Yam, Z. Wang, A replaceable fuse steel-concrete composite connection: force transfer mechanism and design considerations, J. Constr. Steel Res. 183 (2021), 106760.
[21] X. He, K. Ke, Y. Chen, M.C.H. Yam, T. Shao, An experimental study of steel-concrete composite connections equipped with fuse angles, J. Constr. Steel Res. 195 (2022), 107357.
[22] J. Wang, W. Wang, Y. Bao, D. Lehman, Numerical investigation on progressive collapse resistance of steel-concrete composite floor systems, Struct. Infrastruct. Eng. 17 (2021) 202–216.
[23] J. Wang, K. Ke, W. Wang, Structural robustness evaluation of steel frame buildings with different composite slabs using reduced-order modeling strategies, J. Constr. Steel Res. 196 (2022), 107371.
[24] T.W. Francisco, Structural Integrity of the Composite Slab in Steel Gravity Framing Systems, Purdue University, 2014.
[25] M.H. Lai, W. Song, X.L. Ou, M.T. Chen, Q. Wang, J.C.M. Ho, A path dependent stress-strain model for concrete-filled-steel-tube column, Eng. Struct. 211 (2020), 110312.
[26] F.M. Ren, S.Y. Tian, L. Gong, J.L. Wu, J.X. Mo, C.L. Lai, M.H. Lai, Seismic performance of a ring beam joint connecting FTCES column and RC / ESRC beam with NSC, J. Build. Eng. 63 (2023) 105366.
[27] S. Yi, M.T. Chen, B. Young, Design of concrete-filled cold-formed steel elliptical stub columns, Eng. Struct. 276 (2023), 115269.
[28] S. Yi, M.T. Chen, B. Young, Stub column behavior of concrete-filled cold-formed steel semi-oval sections, J. Struct. Eng. 149 (3) (2023) 04023001.
[29] M.H. Lai, Y.H. Lin, Y.Y. Jin, Q. Fei, Z.C. Wang, J.C.M. Ho, Uni-axial behaviour of steel slag concrete-filled-steel-tube columns with external confinement, Thin-Walled Struct. (2023), 110562, https://doi.org/10.1016/j.tws.2023.110562.
[30] H. Li, X. Cai, L. Zhang, B. Zhang, W. Wang, Progressive collapse of steel moment-resisting frame subjected to loss of interior column: experimental tests, Eng. Struct. 150 (2017) 203–220.
[31] H. Li, Modeling, Behavior and Design of Collapse-Resistant Steel Frame Buildings, University of Michigan, 2013.

[32] B.I. Song, H. Sezen, Experimental and analytical progressive collapse assessment of a steel frame building, Eng. Struct. 56 (2013) 664–672.
[33] B.I. Song, K.A. Giriunas, H. Sezen, Progressive collapse testing and analysis of a steel frame building, J. Constr. Steel Res. 94 (2014) 76–83.
[34] J. Wang, W. Wang, Macromodeling approach and robustness enhancement strategies for steel frame buildings with composite slabs against column loss, J. Struct. Eng. 148 (2022) 04021238.
[35] Y. Alashker, H. Li, S. El-Tawil, Approximations in progressive collapse modeling, J. Struct. Eng. 137 (2011) 914–924.
[36] H. Li, S. El-Tawil, Three-dimensional effects and collapse resistance mechanisms in steel frame buildings, J. Struct. Eng. 140 (2014) A4014017.
[37] F. Fu, Progressive collapse analysis of high-rise building with 3-D finite element modeling method, J. Constr. Steel Res. 65 (2009) 1269–1278.
[38] F. Fu, 3-D nonlinear dynamic progressive collapse analysis of multi-storey steel composite frame buildings — parametric study, Eng. Struct. 32 (2010) 3974–3980.
[39] LS-DYNA R11, Keyword User's Manual, LiverMore Software Technology, California, 2018.
[40] Ministry of Housing and Urban-Rural Development of the People''s Republic of China, GB50017–2017. Standard for Design of Steel Structures, China Planning Press, 2017.
[41] Ministry of Housing and Urban-Rural Development of the People''s Republic of China, GB50011–2010. Code for Seismic Design of Buildings, China Architecture & Building Press, 2016.
[42] Ministry of Housing and Urban-Rural Development of the People''s Republic of China, GB50009–2012. Load Code for Design of Buildings, China Architecture & Building Press, 2012.
[43] China Association for Engineering Construction Standardization, CECS 273: 2010. Code for Composite Slabs Design and Construction, China Architecture & Building Press, 2010.
[44] Ministry of Housing and Urban-Rural Development of the People''s Republic of China, JG/T 368-2012. Steel-Bars Truss Deck, Beijing, 2012.
[45] Y. Song, J. Wang, B. Uy, D. Li, Behaviour and design of stainless steel-concrete composite beam-to-column joints, J. Constr. Steel Res. 184 (2021), 106800.
[46] General Administration of Quality Supervision, Inspection and Quarantine of the People's Republic of China, GB1499–2018. Steel for the Reinforcement of Concrete, China Architecture & Building Press, 2018.
[47] Ministry of Housing and Urban-Rural Development of the People''s Republic of China, JGJ114–2014. Technical specification for concrete structures reinforced with welded steel fabric, China Architecture & Building Press, 2012.
[48] Ministry of Housing and Urban-Rural Development of the People''s Republic of China, GB50010–2010. Code for design of concrete structures, China Architecture & Building Press, 2010.
[49] M.H. Lai, K.J. Wu, X. Cheng, J.C.M. Ho, J.P. Wu, J.H. Chen, et al., Effect of fillers on the behaviour of heavy-weight concrete made by iron sand, Constr. Build. Mater. 332 (2022), 127357.
[50] M.H. Lai, Z.H. Chen, Y.H. Wang, J.C.M. Ho, Effect of fillers on the mechanical properties and durability of steel slag concrete, Constr. Build. Mater. 335 (2022), 127495.
[51] M.H. Lai, L. Hanzic, J.C.M. Ho, Fillers to improve passing ability of concrete, Struct. Concr. 20 (2019) 185–197.
[52] M.H. Lai, A.M. Griffith, L. Hanzic, Q. Wang, J.C.M. Ho, Interdependence of passing ability, dilatancy and wet packing density of concrete, Constr. Build. Mater. 270 (2021), 121440.
[53] M.H. Lai, S.A.M. Binhowimal, L. Hanzic, Q. Wang, J.C.M. Ho, Cause and mitigation of dilatancy in cement powder paste, Constr. Build. Mater. 236 (2020), 117595.
[54] M.H. Lai, S.A.M. Binhowimal, L. Hanzic, Q. Wang, J.C.M. Ho, Dilatancy mitigation of cement powder paste by pozzolanic and inert fillers, Struct. Concr. 21 (2020) 1164–1180.
[55] M.H. Lai, W.C. Lao, W.K. Tang, L. Hanzic, Q. Wang, J.C.M. Ho, Dilatancy swerve in superplasticized cement powder paste, Constr. Build. Mater. 362 (2023), 129524.
[56] J. Wang, W. Wang, X. Qian, Progressive collapse simulation of the steel-concrete composite floor system considering ductile fracture of steel, Eng. Struct. 200 (2019), 109701.
[57] J.R. Rice, D.M. Tracey, On the ductile enlargement of voids in triaxial stress fields, J. Mech. Phys. Solids 17 (1969) 201–217.
[58] M.C.H. Yam, K. Ke, B. Jiang, A.C. Lam, Net section resistance of bolted S690 steel angles subjected to tension, Thin-Walled Struct. 151 (2020), 106722.
[59] B. Jiang, M.C.H. Yam, K. Ke, A.C.C. Lam, Q. Zhao, Block shear failure of S275 and S690 steel angles with single-line bolted connections, J. Constr. Steel Res. 170 (2020), 106068.
[60] K. Ke, Y.H. Xiong, M.C.H. Yam, A.C.C. Lam, K.F. Chung, Shear lag effect on ultimate tensile capacity of high strength steel angles, J. Constr. Steel Res. 145 (2018) 300–314.
[61] Z. Luo, Y. Shi, X. Xue, X. Zhou, X. Yao, Nonlinear patch resistance performance of hybrid titanium-clad bimetallic steel plate girder with web opening, J. Build. Eng. 65 (2023) 105703.
[62] Z. Luo, Y. Shi, X. Xue, L. Xu, H. Zhang, Design recommendations on longitudinally stiffened titanium-clad bimetallic steel plate girder, J. Construct. Steel, Res 201 (2023) 107748.
[63] M.T. Chen, A. Cai, M. Pandey, C. Shen, Y. Zhang, L. Hu, Mechanical properties of high strength steels and weld metals at arctic low temperatures, Thin-Walled Struct. (2023), 110543, https://doi.org/10.1016/j.tws.2023.110543.
[64] B.P. Sinha, K.H. Gerstle, L.G. Tulin, Stress-strain relations for concrete under cyclic loading, J. Proc. 61 (1964) 195–212.
[65] V.S. Gopalaratnam, S.P. Shah, Softening response of plain concrete in direct tension, J. Proc. 82 (1985) 310–323.
[66] J.B. Mander, M.J.N. Priestley, R. Park, Theoretical stress-strain model for confined concrete, J. Struct. Eng. 114 (1988) 1804–1826.
[67] Y.H. Bao, Joseph A. Main, Sam-Young Noh, Evaluation of structural robustness against column loss: methodology and application to RC frame buildings, J. Struct. Eng. 143 (2017) 04017066.
[68] ASCE/SEI 7–-16, Minimum Design Loads and Associated Criteria for Buildings and Other Structures (ASCE Standard - ASCE/SEI 7–16), American Society of Civil Engineers, Reston, Virginia, 2017.
[69] B.A. Izzuddin, A.G. Vlassis, A.Y. Elghazouli, D.A. Nethercot, Progressive collapse of multi-storey buildings due to sudden column loss—part I: simplified assessment framework, Eng. Struct. 30 (2008) 1308–1318.
[70] K. Ke, Y.H. Chen, X.H. Zhou, M.C.H. Yam, S.L. Hu, Experimental and numerical study of a brace-type hybrid damper with steel slit plates enhanced by friction mechanism, Thin-Walled Struct. 182 (2023), 110249.
[71] X.H. Zhou, Y.C. Tan, K. Ke, M.C.H. Yam, H.Y. Zhang, J.Y. Xu, An experimental and numerical study of brace-type long double C-section steel slit dampers, J. Build. Eng. 64 (2023), 105555.
[72] X. He, Y. Chen, K. Ke, T. Shao, M.C.H. Yam, Development of a connection equipped with fuse angles for steel moment resisting frames, Eng. Struct. 265 (2022) 114503.
[73] M.T. Chen, Y. Chen, B. Young, Experimental investigation on cold-formed steel elliptical T-joints, Eng. Struct. (2023) 115593, https://doi.org/10.1016/j.engstruct.2023.115593.
[74] K. Ke, X. Zhou, H. Zhang, M.C.H. Yam, L. Guo, Y. Chen, Performance-based-plastic-design of damage-control steel MRFs equipped with self-centring energy dissipation bays, J. Constr. Steel Res. 192 (2022) 107230.
[75] K. Ke, X. Zhou, M. Zhu, M.C.H. Yam, Y. Wang, Seismic evaluation of industrial steel moment resisting frames with shape memory alloys using performance-spectra-based method, J. Build. Eng. 48 (2022) 103950.
[76] K. Ke, W. Wang, M.C.H. Yam, L. Deng, Residual displacement ratio demand of oscillators representing HSSF-EDBs subjected to near-fault earthquake ground motions, Eng. Struct. 191 (2019) 598–610.
[77] K. Ke, M.C.H. Yam, L. Deng, Q. Zhao, A modified DEB procedure for estimating seismic demands of multi-mode-sensitive damage-control HSSF-EDBs, J. Construct. Steel Res. 150 (2018) 329–345.
[78] X. Xue, Y. Shi, X. Zhou, J. Wang, Y. Xu, Experimental study on the properties of Q960 ultra–high–strength steel after fire exposure, Structures 47 (2023) 2081–2098.
[79] J. Hua, F. Wang, X. Xue, Y. Sun, Y. Gao, Post-fire ultra-low cycle fatigue properties of high-strength steel via different cooling methods, Thin-Walled Struct. 183 (2023) 110406.
[80] H. Fang, Q.Y. Li, T.M. Chan, B. Young, Behaviour and design of high-strength octagonal CFST short columns subjected to combined compression and bending, J. Constr. Steel Res. 200 (2023) 107679.
[81] J. Liu, H. Fang, T.M. Chan, Numerical investigation on local buckling behaviour of cold-formed high strength steel irregular hexagonal hollow section stub columns, Thin-Walled Struct. 185 (2023) 110571.
[82] M.T. Chen, B. Young, Tests of cold-formed normal and high strength steel tubes under tension, Thin-Walled Struct. 153 (2020) 106844.
[83] X.M. Lin, M.C.H. Yam, K. Ke, Q. He, K.F. Chung, Investigation of block shear strength of high strength steel bolted connections, J. Constr. Steel Res. 196 (2022) 107407.
[84] K. Ke, M. Zhang, M.C.H. Yam, A.C.C. Lam, J. Wang, B. Jiang, Block shear performance of double-line bolted S690 steel angles under uniaxial tension, Thin-Walled Struct. 171 (2022) 108668.